

激光增材制造铜铬锆合金研究进展:成形行为、微观组织和综合性能(特邀)

陈兴宇^{1,2}, 李昊^{1,2}, 陈乔雨^{1,2}, 徐海升³, 谢凡轩^{1,2}, 李正^{1,2}, 黄田野⁴, 关凯⁵, 尹作为^{1,2}, 郝亮^{1,2}, 殷杰^{1,2*}

¹中国地质大学(武汉)珠宝学院, 湖北 武汉 430074;

²中国地质大学(武汉)先进制造研究所, 湖北 武汉 430074;

³湖北三江航天江北机械工程有限公司, 湖北 孝感 432000;

⁴中国地质大学(武汉)机械与电子信息学院, 湖北 武汉 430074;

⁵鑫精合激光科技有限公司, 北京 102200

摘要 铜铬锆(CuCrZr)作为沉淀硬化合金,以其良好的耐热性、耐腐蚀性以及优异的力学、电学和热学性能而被广泛应用于航空航天、核能化工等领域。然而,CuCrZr是当前激光增材制造(LAM)难成形材料之一,相关研究报道还很有限。本文综述了近年来激光粉末床熔融(L-PBF)制备CuCrZr合金的研究进展,重点探究了绿激光与近红外激光对成形质量的影响规律,分析了热处理及构建方向与微观组织、力学性能的内在联系,并研究了热处理对于电学、热学性能的强化机制。近红外激光制备样品的致密度波动范围大(95.5%~99.9%),绿激光制备样品的整体致密度较低但波动范围较小(96.5%~98.5%),工艺参数仍有优化空间。合金的微观组织和综合性能都存在各向异性,即沿水平方向的晶粒细小,沿垂直方向的晶粒为柱状晶粒。固溶处理会使合金的熔池边界消失并改变晶粒形态,时效处理导致合金产生沉淀并改变晶粒取向。500℃左右处理1~2h的直接时效处理对力学性能的提升最大,时效处理通过降低位错密度、减少热残余应力和促进沉淀物的形成,显著增强了合金的力学性能。对电学、热学性能提升最大的热处理条件为950~1000℃的固溶退火处理1h+500℃左右的时效硬化处理1~3h,这是因为固溶退火+时效硬化处理降低了位错密度和残余应力,并产生了有益的沉淀物。本文总结了L-PBF制备CuCrZr合金的成形行为、微观组织和综合性能的研究进展,并对其研究前景和发展方向进行了展望。

关键词 激光增材制造; 铜铬锆合金; 成形行为; 微观组织; 综合性能

中图分类号 TG146.11; TG665 **文献标志码** A

DOI: 10.3788/CJL231437

1 引言

激光增材制造(LAM)因具有高精度且能制造复杂结构的部件而被广泛应用于各个行业领域^[1-2]。LAM技术一般分为激光定向能量沉积(LP-DED)和激光粉末床熔融(L-PBF)两类。其中,L-PBF技术目前发展迅速,在科学研究及工业生产中备受青睐^[3]。

铜是人类最早掌握使用的金属之一,其冶炼技术的发展标志着人类从石器时代进入了青铜时代。铜及铜合金具有高导电性、高导热性及优异的力学性能^[4-5],是当前国家的重要战略储备并在国民经济中具有重要的地位。近年来,随着对复杂功能性铜及铜合金部件的需求不断增加,LAM铜及铜合金已成为研究热点^[6-7],但其热导率高和对近红外激光的反射率高,是LAM难成形的材料之一^[8]。目前,对纯铜^[9]、黄

铜^[10]、青铜^[11]、白铜^[12]等的研究较为充分,但是对CuCrZr合金的综合性研究却相对缺乏。

CuCrZr合金是一种沉淀硬化合金,属于高铜合金,添加Cr元素能提升其力学性能,而添加Zr元素能抑制Cr沉淀相生长、改善沉淀相的分布从而提高性能,并且微量Zr元素对电导率的影响非常小^[13-14]。如图1所示,CuCrZr合金的优异特性使其能广泛应用于多个领域:1) CuCrZr合金具有良好的耐热性和高强度特性^[15],并且在高温环境下能保持较好的稳定性,是制造耐高温零件的理想材料,如航空航天发动机喷管、燃烧室壁板等^[16];2) CuCrZr合金对氧化、腐蚀和高温气体侵蚀具有较好的抵抗能力,因此它在一些腐蚀性环境中的应用非常广泛,如化工设备、海洋工程、核工业等^[17-18];3) CuCrZr合金具有优异的导电性和导热性^[19-20],是制造电气零部件和散热器的理想选择^[21];

收稿日期: 2023-11-27; 修回日期: 2023-12-29; 录用日期: 2024-01-17; 网络首发日期: 2024-01-25

基金项目: 国家自然科学基金(61805095)、装备预研教育部联合基金创新团队项目(8091B042207)、湖北省揭榜制科技项目(2021BEC010)、湖北省珠宝工程技术研究中心基金(CIGTXM-03-202307)、中央高校基本科研业务费专项(2021239)

通信作者: *yinjie@cug.edu.cn

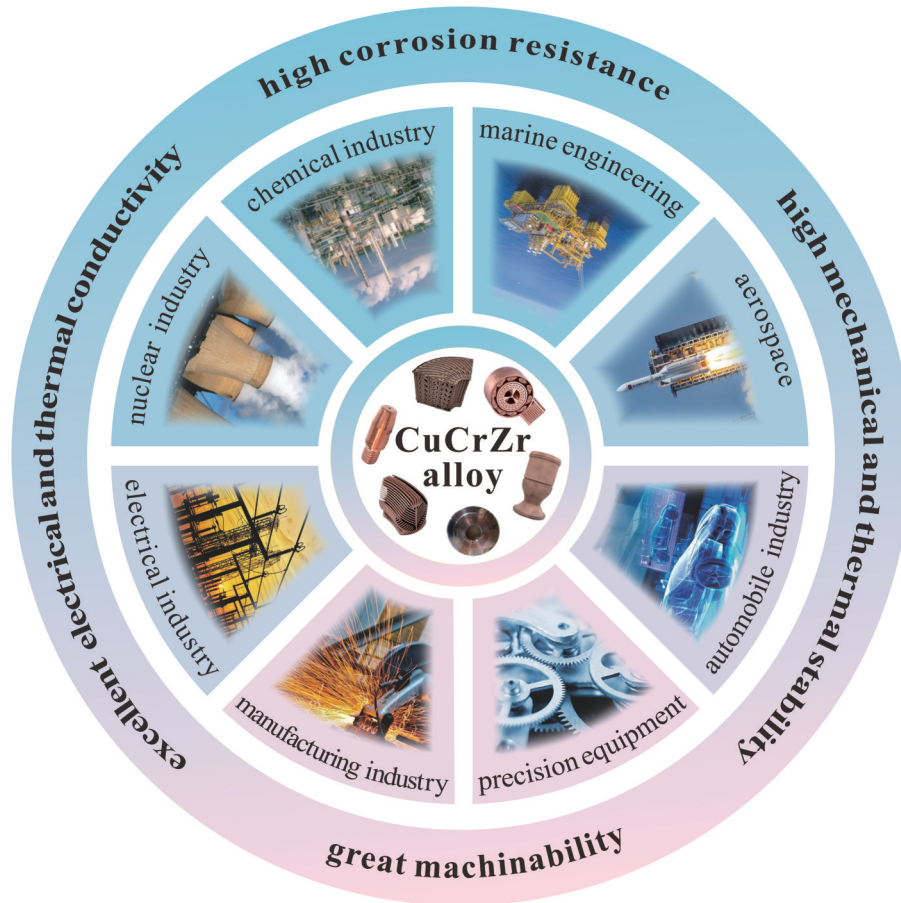


图 1 CuCrZr 合金的特性及应用领域

Fig. 1 Characteristics and application areas of CuCrZr alloys

4) CuCrZr 合金具有较好的可加工性,能通过增材制造技术(如 L-PBF、LP-DED)成形^[22],且具有良好的焊接性,便于制造和组装具有复杂结构的零部件。

当前,C18150 和 C18160(含 Fe、Si 元素)两种合金是 CuCrZr 合金中的热点研究牌号,其化学成分及含量如表 1 所示。研究人员通过 L-PBF 制备得到的 CuCrZr 合金的致密度都已超过 97%,其中使用近红外激光(波长在 1064 nm 附近)制备的试样的致密度范围为 97.6%~99.9%^[20,23-24],而使用绿激光(波长为 515 nm)制备的试样的致密度范围为 98.0%~99.1%^[25-26]。对使用近红外激光制备 CuCrZr 合金的研究已较为充分,而对使用绿激光制备 CuCrZr 合金的研究还很有限。

表 1 常规牌号 CuCrZr 合金的化学组成^[27]

Table 1 Chemical composition of regular grades of CuCrZr alloys^[27]

Alloy grade	Mass fraction / %				
	Cu	Cr	Zr	Fe	Si
C18150	Balance	0.50-1.50	0.02-0.20	-	-
C18160	Balance	0.20-1.20	0.05-0.25	0.1	0.1

微观组织方面,使用 L-PBF 制备的 CuCrZr 合金微观组织存在各向异性,时效处理对微观组织的影响很小,而固溶处理会导致熔池边界消失,这是因为

CuCrZr 合金固溶处理温度(800~1000 °C)^[20,25]远高于时效处理温度(400~600 °C)^[16,28]。沉积态下,Cr、Zr 原子在合金基体中过饱和,经时效硬化处理后 CuCrZr 合金的主要沉淀相为 Cr、Cu₂Zr_y^[29]和 Cr₂Zr^[16]。经一定条件时效处理后的试样的晶粒取向发生明显变化,沿 [100] 及 [111] 方向的取向减弱,沿 [110] 方向的取向增强^[25]。

力学性能方面,多数研究者^[20,23-24,26,28]使用近红外激光制备的 CuCrZr 合金沉积态试样的屈服强度、极限拉伸强度分别在 180~270 MPa 和 254~338 MPa 范围内,延展率在 20.5%~49.4% 范围内,但 Tang 等^[25]使用绿激光制备的沉积态试样的屈服强度、极限拉伸强度分别达到 400 MPa、447 MPa,不过延展率仅有 10%。时效处理极大地提高了试样的屈服强度、极限拉伸强度,却牺牲了延展率(降至 12.3%~21.8%)。在时效处理后,屈服强度和极限拉伸强度分别提升到 361~527 MPa 及 466~612 MPa^[20,23-24,26,28]。热学、电学性能方面,目前的相关研究还不多:沉积态试样的电导率仅在 14% IACS~30% IACS,而经热处理后达到 41% IACS~90% IACS^[16,20,26,30-31];沉积态试样的热导率为 100~125 W/(m·K),在热处理后可提升到 297~350 W/(m·K)^[24-25,31]。然而,目前尚未有研究找到力学、电学及热学性能之间的最佳平衡,综合性能的研究尚未充分。

目前, CuCrZr 合金已经成为 LAM 的研究前沿, 但有关的研究报道特别是综述论文还很有限^[32], 阻碍了 LAM 制备 CuCrZr 合金在航空航天、能源等领域的深入应用, 表现在: 首先, 绿激光/近红外激光对成形行为的影响规律还未完全探明; 其次, LAM 制备 CuCrZr 合金的力学、电学及热学综合性能的调控机理尚未厘清。针对以上问题, 本文综述了 L-PBF 制备 CuCrZr 合金在国内外的研究进展, 系统地总结了 CuCrZr 合金的成形行为、微观组织, 以及力学、热学和电学性能, 探讨了

CuCrZr 合金研究面临的挑战, 最后对 LAM 制备 CuCrZr 合金的未来发展方向进行了展望。

2 CuCrZr 合金成形的研究进展

CuCrZr 合金的高致密成形是微观组织和综合性能研究的前提, 本节从工艺参数及激光波长等方面对成形行为的影响因素进行探讨。图 2 所示为本团队使用的 L-PBF 增材制造设备(天津镭明激光 LiM-X260A)、打印原理示意图及所制备的 CuCrZr 合金试样。

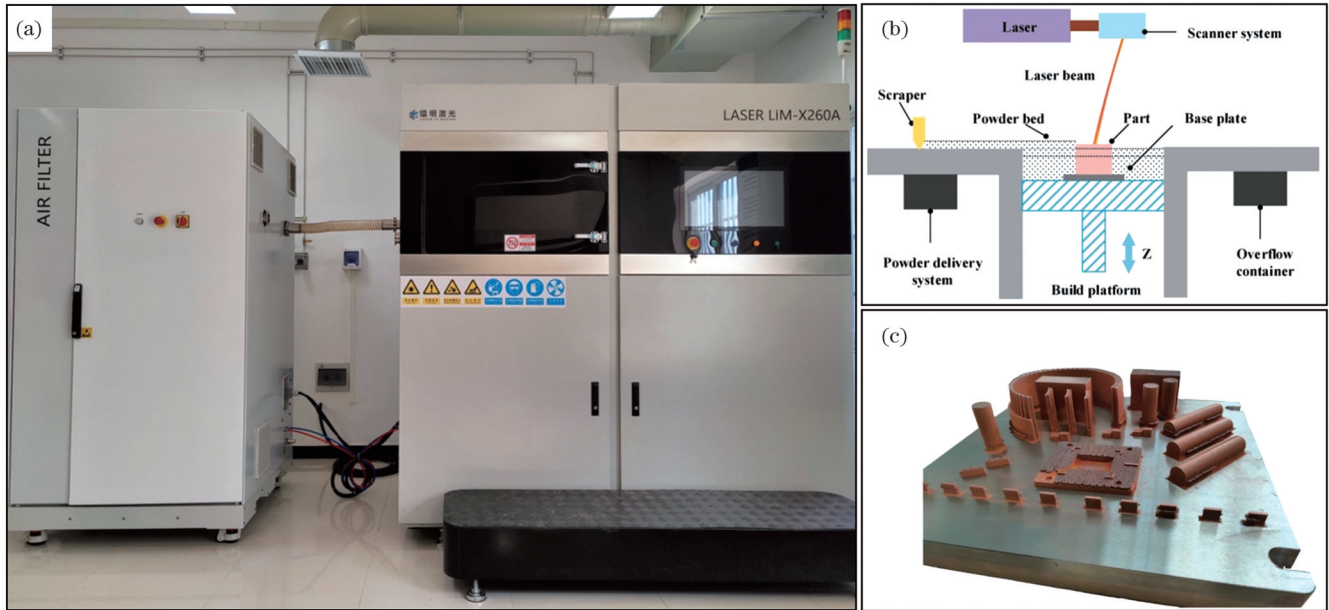


图 2 L-PBF 设备、打印原理及所制备的试样。(a)L-PBF 增材制造设备(天津镭明激光 LiM-X260A); (b)L-PBF 打印原理示意图^[33]; (c)L-PBF 制备的 CuCrZr 合金试样

Fig. 2 L-PBF equipment, printing principle, and prepared sample. (a) LiM-X260A L-PBF additive manufacturing equipment; (b) schematic of L-PBF printing principle^[33]; (c) CuCrZr alloy sample prepared by L-PBF

2.1 工艺参数对 CuCrZr 合金成形质量的影响

激光功率(P)、扫描速度(v)、扫描间距(h)及粉床厚度(d)是 L-PBF 成形 CuCrZr 合金的主要工艺参数^[34-35]。本文在传统体积能量密度的基础上^[36], 针对铜及铜合金对激光波长吸收率的敏感性(对 515 nm 波长激光的吸收率为 0.74, 对 1064 nm 波长激光的吸收率为 0.18)^[25], 提出了考虑吸收率(A)的体积能量密度(E_A)来探究工艺参数对 CuCrZr 合金成形的影响, 其计算公式为

$$E_A = \frac{AP}{vdh} \quad (1)$$

如图 3 所示, 近红外激光的 E_A 为 20~200 J/mm³, 而绿激光的 E_A 为 100~500 J/mm³, 这是因为 CuCrZr 合金对绿激光的吸收率远高于对近红外激光的吸收率。近红外激光制备样品的致密度为 95.5%~99.9%, 波动范围大, 而绿激光制备样品的致密度为 96.5%~98.5%, 在吸收率优于近红外激光的条件下绿激光制备样品的致密度还低于近红外激光制备样品, 说明绿激光工艺参数仍有优化空间。在使用近红外激光的研

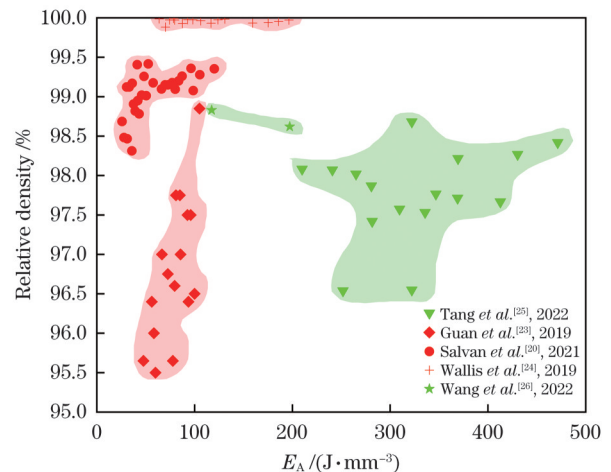


图 3 不同 L-PBF 实验中 E_A 与致密度的关系(使用近红外激光制备得到的试样的图例为红色, 使用绿激光制备得到的试样的图例为绿色)

Fig. 3 Relationship between E_A and density in different L-PBF experiments (the legend for samples prepared by near-infrared laser is red and the legend for samples prepared by green laser is green)

究中: Guan 等^[23]得到致密度为 97.6% 的试样; Salvan 等^[20]制备了致密度最高为 99.4% 的试样, 并发现激光功率对致密度的影响最大; Wallis 等^[24]得到致密

度最高为 99.9% 的试样, 发现激光功率对致密度的影响大于扫描速度。上述研究中的详细工艺参数如表 2 所示。

表 2 各研究中最高致密度样品所使用的工艺参数
Table 2 Process parameters used for the highest density samples in each study

Optimal process parameter				Wavelength / nm	$E_A / (J \cdot mm^{-3})$	Density / %	Ref.
Laser power / W	Laser scanning speed / $(mm \cdot s^{-1})$	Hatching distance / μm	Layer thickness / μm				
400	300	80	30	515	411.1	99.1	Wang <i>et al.</i> ^[26] , 2022
485	400	90	30		Tang <i>et al.</i> ^[25] , 2022		
500	700	50	40		64.3	99.9	Yang <i>et al.</i> ^[16] , 2023
425	650	110	-		-	99.2	Ma <i>et al.</i> ^[37] , 2022
425	350	90	30	1064	80.9	97.6	Guan <i>et al.</i> ^[23] , 2019
370	500	80	20		83.3	99.9	Wallis <i>et al.</i> ^[24] , 2019
480	700	100	30		41.1	99.4	Salvan <i>et al.</i> ^[20] , 2021

由图 3 可知, Tang 等^[25]使用 515 nm 波长的绿激光得到了致密度为 98.6% 的试样。Wang 等^[38]使用相同波长的绿激光得到了致密度为 99.1% 的试样, 如图 4 所示, 他们使用 OLYMPUS 金相显微镜观察发现, 在激光功率不变的条件下, 随着扫描速度和扫描间距的增加, 致密度下降、孔隙增大。使用绿激光制备样品时激光功率仍是对致密度影响最大的参数。Ma 等^[39]和周吉强等^[34]采用方差分析(ANOVA)的实

验方法来优化工艺参数^[40], 他们都发现使用近红外激光制备 CuCrZr 合金试样时, 激光功率对试样的致密度影响最大。此外, 无论是使用近红外激光还是使用绿激光, 扫描速度对致密度都具有显著影响^[35]。目前, 使用绿激光制备 CuCrZr 合金的致密度低于使用近红外激光制备合金的致密度, 说明对使用绿激光制备 CuCrZr 合金的工艺参数的研究还不够充分。

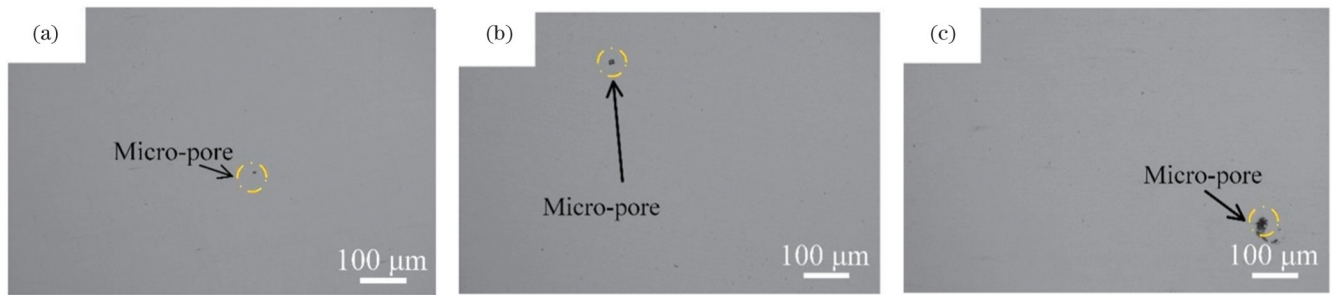


图 4 CuCrZr 合金样品在金相显微镜下观察的图片^[38]。(a)致密度为 99.15% 的样品; (b)致密度为 98.83% 的样品; (c)致密度为 98.62% 的样品

Fig. 4 Metallurgical microscopes diagrams of CuCrZr alloy samples^[38]. (a) Sample with 99.15% density; (b) samples with 98.83% density; (c) sample with 98.62% density

2.2 激光波长对 CuCrZr 合金成形的影响

由于 Cu 及 Cu 合金具有对近红外激光的高反射率、在高温下易氧化及高热导率等特性, 因此在使用 LAM 制备 Cu 及 Cu 合金时存在许多挑战。近红外激光熔化 Cu 及 Cu 合金的过程中低的能量吸收率导致金属粉末熔化困难, 进而导致未熔合等缺陷和成形效率低等问题。从图 5 可以看出, 纯 Cu 及 CuCrZr 合金粉末对 515 nm 处绿激光的吸收率远高于对 1064 nm 处近红外激光的吸收率。良好的吸收率意味着能提高制备的稳定性和效率, 所以近年来开始有学者用绿激光

代替近红外激光制备 CuCrZr 合金^[26, 31]。

如图 5 所示, 纯 Cu 和 CuCrZr 合金对激光的吸收率随激光波长的增加单调递减, 在激光波长超过 550 nm 后吸收率急剧下降, Cr、Zr 的添加使得粉末对激光的吸收率增大。Tang 等^[25]发现 Cr 和 Zr 元素的添加提高了 Cu 对激光的吸收率。目前, 使用绿激光制备 CuCrZr 合金从工艺参数的优化到对试样的微观组织及性能的研究等方面都远不如用近红外激光制备的合金。当前采用绿激光和近红外激光打印 CuCrZr 合金试样的最优工艺参数如表 2 所示。

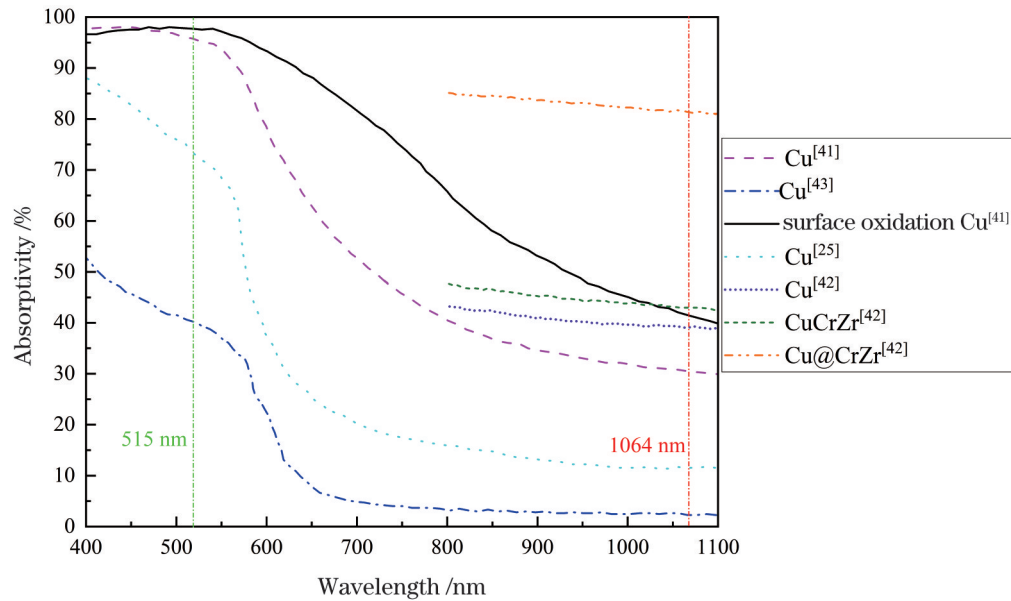


图5 CuCrZr粉末、纯Cu粉末、表面氧化的Cu粉末和具有CrZr涂层的Cu粉末(标记为Cu@CrZr)对激光的吸收率

Fig. 5 Absorptivity rate of laser by CuCrZr powder, pure Cu powder, surface-oxidized Cu powder, and Cu powder with CrZr coating (Cu@CrZr)

通过图5还发现,采用粉末表面改性处理也能有效提高激光吸收率。Lassègue等^[42]在铜粉表面形成均匀的CrZr涂层后,测试发现有CrZr涂层的Cu粉末在1064 nm处的吸收率达到0.81,远高于未处理时的0.39。同样,Brandau等^[41]在对纯Cu(在1064 nm处的吸收率为0.31)进行表面氧化处理后(在1064 nm处的吸收率为0.41)也显著提升了粉末对激光的吸收率。

2.3 缺陷对CuCrZr合金成形的影响

缺陷是L-PBF合金高质量成形的重要影响因素,本文根据前人研究将L-PBF中的缺陷分为两类,分别是表面缺陷和内部缺陷,图6所示为L-PBF成形CuCrZr合金中的各种缺陷^[44]。

表面缺陷是指样品不均匀或不规则的表面特征。导致LAM部件表面缺陷的因素主要有三种,分别是台阶效应、粉末未完全熔化和球化效应。阶梯效应是指由加工精度有限导致的曲面和倾斜面层近似为阶梯状。如图6(a)所示,球化效应是增材制造中十分常见的问题,甚至是造成金属增材制造中样品表面缺陷和孔隙的主要原因之一。Bai等^[45]在制备CuCrZr样品中观察到球化效应,当输入能量较低时,热源只能熔化部分表面粉末,无法穿透至粉层下部,粉层与基板之间存在大量孔隙,此时松散的粉层对熔池几乎没有约束力,表面张力起决定作用,而液滴有形成最小表面的倾向,液滴由此形成球形,产生球化现象^[46-47]。如图6(b)所示,粉末未完全熔化是指在增材制造过程中使用低能量输入时,粉末可能部分熔化并粘附到零件表面^[48-49]。

内部缺陷分为内部裂纹和孔隙。增材制造中形成

的内部裂纹主要有两种,分别是热裂纹和固态裂纹。图6(f)所示为LAM制备CuCrZr合金中产生的裂纹^[50]。热裂纹产生于凝固或热循环过程中相对较高的温度下,并且热裂纹也有两种,分别为凝固裂纹和液化裂纹。热裂纹的产生需要两个条件:存在液膜和过大的热应力。凝固裂纹一般出现在凝固熔池内的凝固近端阶段,枝晶生长成完整的晶粒,剩余液体的流动受到凝固枝晶阻碍,导致液体金属不能充分地供应到枝晶空间中。同时,凝固收缩和热收缩产生拉应力/应变,并集中在液膜附近,当局部拉伸应力/应变超过材料抗开裂阈值时,发生凝固开裂。液化裂纹发生在热影响区,在LAM的热循环过程中,当热影响区被加热到较高温度时,低熔点相的重熔导致液膜沿着晶界或在晶内形成。由于热循环过程中产生的热应力较大,液体膜成为裂纹产生的场所,并加速裂纹沿着晶界扩展。固态裂纹产生于相对较低的温度下,出现这种情况的原因是金属的脆性和增材制造工艺中热循环引起的巨大残余应力^[51]。

L-PBF金属零件的内部孔隙可分为熔合不足孔隙、冶金孔隙、匙孔孔隙和收缩孔隙。这4种典型的L-PBF零件内部孔隙如图6(c)、(d)、(e)所示。熔合不足孔隙的产生是因为输入的能量较低,熔池较小且较浅,无法充分渗透到底板或之前制造的层中^[47]。冶金孔隙的产生是因为凝固的熔池中夹带气体,而高冷却速度会阻碍内部气体及时逸出,这种孔隙是L-PBF金属和合金所固有的,无法完全消除^[52]。匙孔孔隙则是由不稳定的熔化模式引起的^[53]。最后一种内部孔隙是收缩孔隙,它是凝固过程结束时,残余液体在枝晶间区域隔离而形成的^[54]。

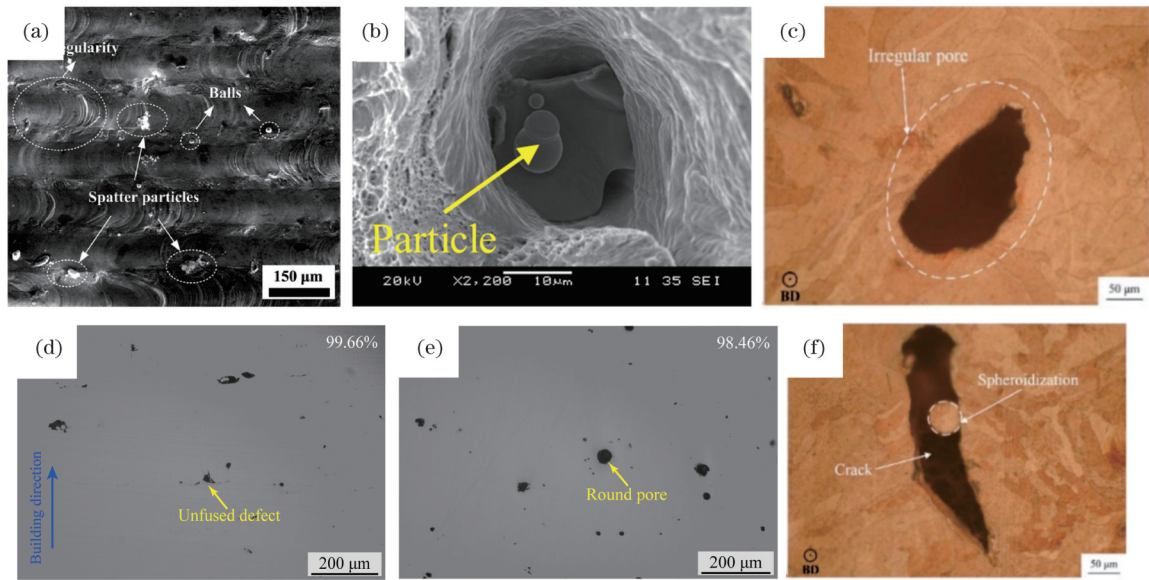


图 6 LAM 制备 CuCrZr 样品中的缺陷。(a)球化效应^[39]；(b)粉末未完全熔化^[45]；(c)不规则孔隙^[50]；(d)未熔合孔隙^[16]；(e)冶金孔隙^[16]；(f)裂纹^[50]

Fig. 6 Defects in LAM-fabricated CuCrZr samples. (a) Balling effect^[39]; (b) partially melted powders^[45]; (c) irregular pores^[50]; (d) lack of fusion pores^[16]; (e) metallurgical pores^[16]; (f) crack^[50]

3 CuCrZr 合金的微观组织研究进展

3.1 沉积态 CuCrZr 合金的微观组织

L-PBF 制备的 CuCrZr 合金微观组织存在各向异性,该合金因其高的热导率优先在高热梯度的方向形成柱状结晶,并且晶体的长轴方向与热方向一致^[45]。沉积态的试样沿水平方向可见弯曲破碎的晶粒,沿垂直方向可见柱状晶粒。

如图 7 所示,Salvan 等^[20]分析了沉积态 CuCrZr 合金试样的微观组织,发现沿水平方向与沿垂直方向的晶粒形状有较大区别,样品的晶粒沿垂直方向拉长,沿水平方向的晶粒则更细小。Wang 等^[26]观察了金相显微镜下水平与垂直方向上沉积态 CuCrZr 合金试样的微观组织,沿垂直方向的晶粒相对细长,呈现柱状晶体的特征,而沿水平方向的晶粒相对较小。Ma 等^[39]同样观察到 CuCrZr 合金试样的晶粒沿着垂直方向生长,并且

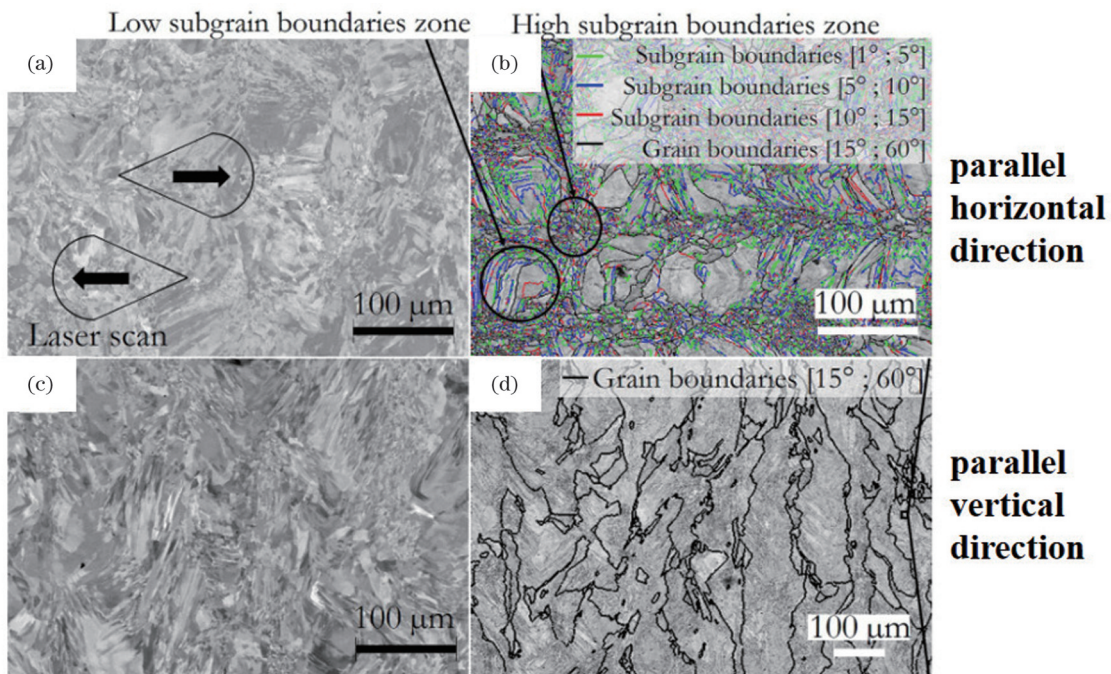


图 7 激光粉末床熔融 CuCrZr 样品的 SEM 图像^[20]。(a)(b)沿水平方向的微观组织；(c)(d)沿垂直方向的微观组织

Fig. 7 SEM images of as-built L-PBF CuCrZr sample^[20]. (a)(b) Microstructure in horizontal building direction; (c)(d) microstructure in vertical building direction

晶粒尺寸不均匀,沿水平方向的晶粒尺寸更小、更均匀。

如图 8 所示,L-PBF 沉积态试样及合金粉末的最强衍射峰位置不同,合金粉末的最强峰出现在 $2\theta=43.27^\circ$ 的 $\{111\}$ 衍射峰位置,而沉积态的最强峰出现在 $2\theta=74.05^\circ$ 的 $\{220\}$ 衍射峰处,在该位置附近沉积态试样的峰位相较于合金粉末向左偏移较小的角度。在 L-PBF 制备 CuCrZr 合金的过程中,晶粒在熔池内温度梯度的影响下择优生长形成织构,所以 X 射线衍射仪 (XRD) 测试的最强峰位置在成形前后会发生变化^[39]。L-PBF 成形过程中冷却速率高,导致 Cr 和 Zr 在 Cu 基体中的固

溶度增加,造成 CuCrZr 合金晶粒出现晶格畸变现象,同时试样中存在的残余应力使得晶面间距变大,所以 XRD 测试图谱的峰值位置向低角度方向偏移^[26]。

对 LAM 银合金的研究中同样发现类似的织构变化。Xiong 等^[55]对 925 银的研究发现,相较于粉末,L-PBF 之后的样品 XRD $\{111\}$ 晶面峰值减小, $\{220\}$ 晶面峰值同样降低。Vikram 等^[56]对 925 银的研究发现,相比于铸造的样品,LAM 的样品 $\{111\}$ 晶面峰值更大, $\{200\}$ 晶面峰值显著低于铸造样品, $\{220\}$ 晶面峰值则略高。

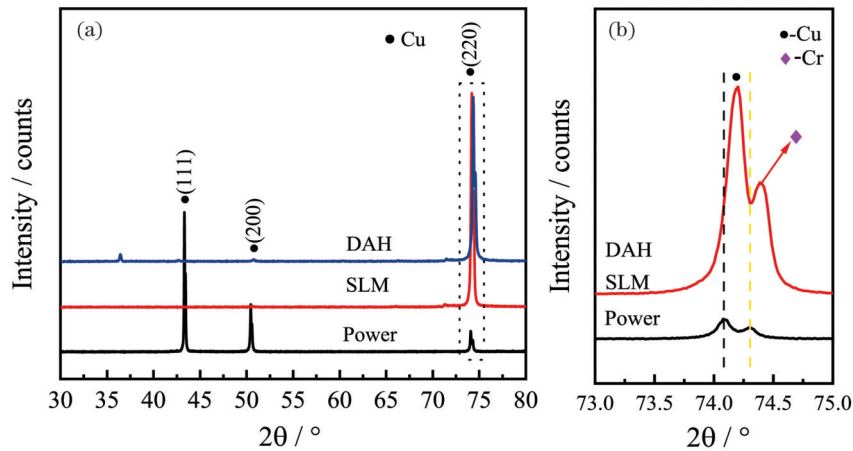


图 8 XRD 谱图^[26]。(a)CuCrZr 合金粉末及 L-PBF 合金;(b) $73^\circ\sim 75^\circ$ 局部放大图

Fig. 8 XRD patterns^[26]. (a) CuCrZr alloy powder and L-PBF alloy; (b) $73^\circ\sim 75^\circ$ localized magnification

3.2 热处理对 CuCrZr 合金微观组织的影响

时效处理对试样的微观组织影响不大,而固溶处理后,试样的熔池边界消失,晶粒形态也发生了变化。这可归因于固溶处理的温度更高,而更高的热处理温度对试样的微观组织有着更大的影响^[28]。

如图 9、图 10 所示,Bai 等^[45]观察发现,经热处理后试样熔池边界消失,同时细长和弯曲的晶粒消失,取而代之的是多边形晶粒。固溶处理 (ST) 试样和固溶时效 (SAT) 试样的微观组织类似,其中都存在细小及粗大的晶粒,沿垂直方向与沿水平方向试样的微观组织变化类似。Kuai 等^[28]对沉积态 (AB)、ST、SAT 和直接时效 (DA) 试样沿水平方向的平面进行观察,AB 和 DA 试样都存在熔池边界,并且晶粒大小差异没有统计学意义,而 ST 和 SAT 试样中的熔池边界消失。Yang 等^[16]发现时效处理后,蜂窝状亚结构的边界出现了许多沉淀物,一些小尺寸的沉淀物发生聚集。

热处理的温度和时间对沉淀的数量和种类都有较大影响。在时效处理后 CuCrZr 合金的主要沉淀相为 Cr、 Cu_5Zr_3 和 Cr_2Zr ,随着热处理温度的增加,沉淀的分布方式也会发生变化。

Zeng 等^[57]采用 CALPHAD 方法进行热力学计算^[58],计算结果如图 11 所示,在平衡状态下,CuCrZr 合金的主要相为铜相 (FCC_L12)。CuCrZr 合金中的

沉淀物包括 Cr (BCC_B2)、 Cr_2Zr (C15_LAVES) 和 $\text{Cu}_{51}\text{Zr}_{14}$,但在 630°C 时, $\text{Cu}_{51}\text{Zr}_{14}$ 会转变为 Cr_2Zr 。

如图 12 所示,Yang 等^[16]观察到随着时效温度的升高,Cr 沉淀相的尺寸逐渐增大。如图 13 所示,使用 TEM-EDS 进行分析,发现在 480°C 时效处理的试样中观察到均匀的 Cr 沉淀物,这些沉淀物的晶体结构与 Cu 基体相同,并形成相干界面和 Guinier Preston 区^[59],而在 580°C 时效处理的试样中,沉淀物发生了聚集现象。如图 14 所示,Salvan 等^[20]在直接时效硬化 (DAH) 处理后,在 Cr 沉淀物中观察到类似现象。在晶界处,Zr 沉淀物在 Cr 纳米沉淀物旁边,而在 Cu 基体内部显示为六方沉淀物。

热处理后,使用 XRD 对试样进行分析,发现试样的最强衍射峰位置较沉积态向左微弱偏移。衍射峰位置的偏移,表明晶格单元的增加是由热处理过程中 Cu 基体中 Cr 的溶解和沉淀造成的^[60-61],时效处理的温度和时间对试样的晶粒取向有很大的影响。

如图 15 所示,Tang 等^[25]发现热处理后 $\{111\}$ 衍射峰向左微弱偏移,固溶退火+时效硬化处理、固溶退火处理,以及低温、短时间的直接时效硬化处理对晶粒取向的影响不大。在 $500^\circ\text{C}\times 2\text{h}$ 及 $550^\circ\text{C}\times 1\text{h}$ 的直接时效硬化处理后,沿着 $\{111\}$ 及 $\{200\}$ 晶面的强度变弱,平行于 $\{220\}$ 晶面的强度增加,这说明该热处理条件对试样晶粒取向有很大影响。Wang 等^[26]在热处理条件

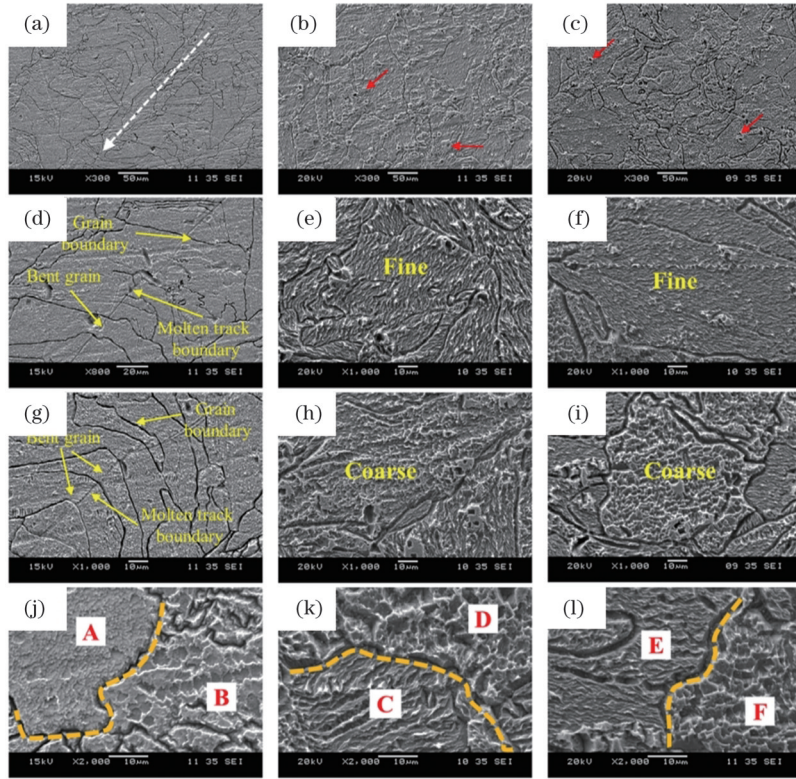


图9 使用扫描电子显微镜观察 CuCrZr 合金水平方向的微观结构^[45]。(a)(d)(g)(j)AB(沉积态)试样的微观组织;(b)(e)(h)(k)ST(固溶处理)试样的微观组织;(c)(f)(i)(l)SAT(固溶时效处理)试样的微观组织

Fig. 9 Microstructure of horizontal direction of SLMed CuCrZr alloy by SEM^[45]. (a)(d)(g)(j) Microstructure of AB samples; (b)(e)(h)(k) microstructure of ST samples; (c)(f)(i)(l) microstructure of SAT samples

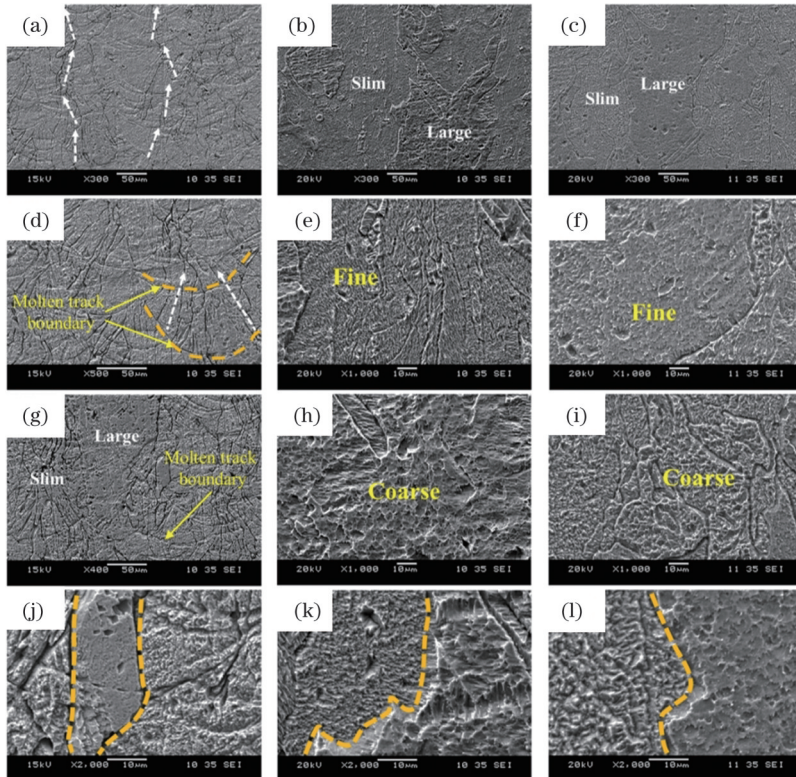


图10 使用扫描电子显微镜观察 CuCrZr 合金构建方向的微观结构^[45]。(a)(d)(g)(j)AB(沉积态)试样的微观组织;(b)(e)(h)(k)ST(固溶处理)试样的微观组织;(c)(f)(i)(l)SAT(固溶时效处理)试样的微观组织

Fig. 10 Microstructure of building direction of SLMed CuCrZr alloy by SEM^[45]. (a)(d)(g)(j) Microstructure of AB samples; (b)(e)(h)(k) microstructure of ST samples; (c)(f)(i)(l) microstructure of SAT samples

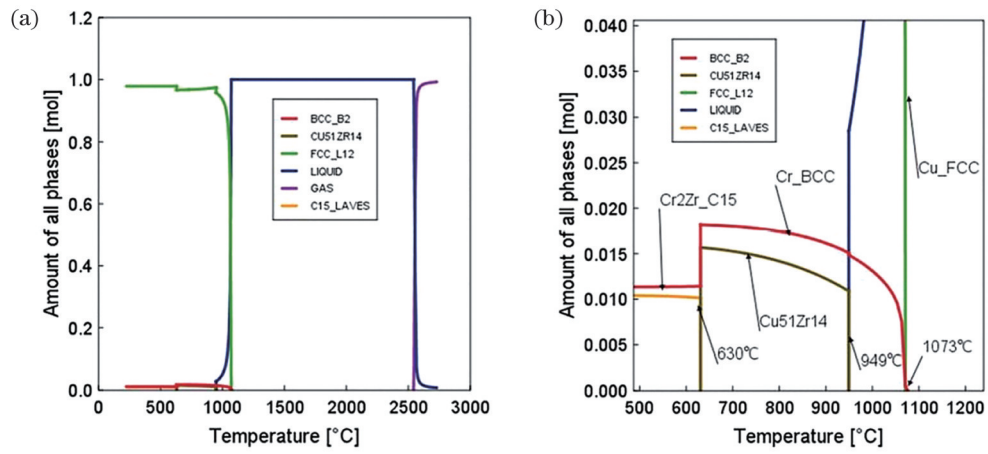


图 11 CuCrZr 合金的 CALPHAD 热力学计算结果^[29]。(a) 全范围计算结果；(b) 次要相位

Fig. 11 Thermodynamics calculation results of CuCrZr alloys using CALPHAD^[29]. (a) Full range calculation results; (b) minor phases

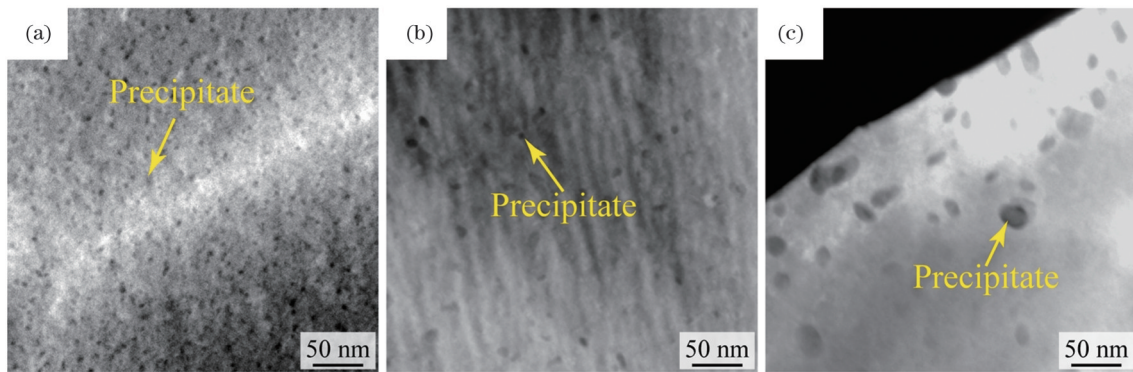


图 12 DA 试样的高角度环形暗场 (HAADF) 分析^[16]。(a) 480 °C 时效处理 4 h 样品；(b) 530 °C 时效处理 4 h 样品；(c) 580 °C 时效处理 4 h 样品

Fig. 12 High-angle annular dark field (HAADF) analysis of DA samples^[16]. (a) Aging treatment samples at 480 °C for 4 h; (b) aging treatment samples at 530 °C for 4 h; (c) aging treatment samples at 580 °C for 4 h

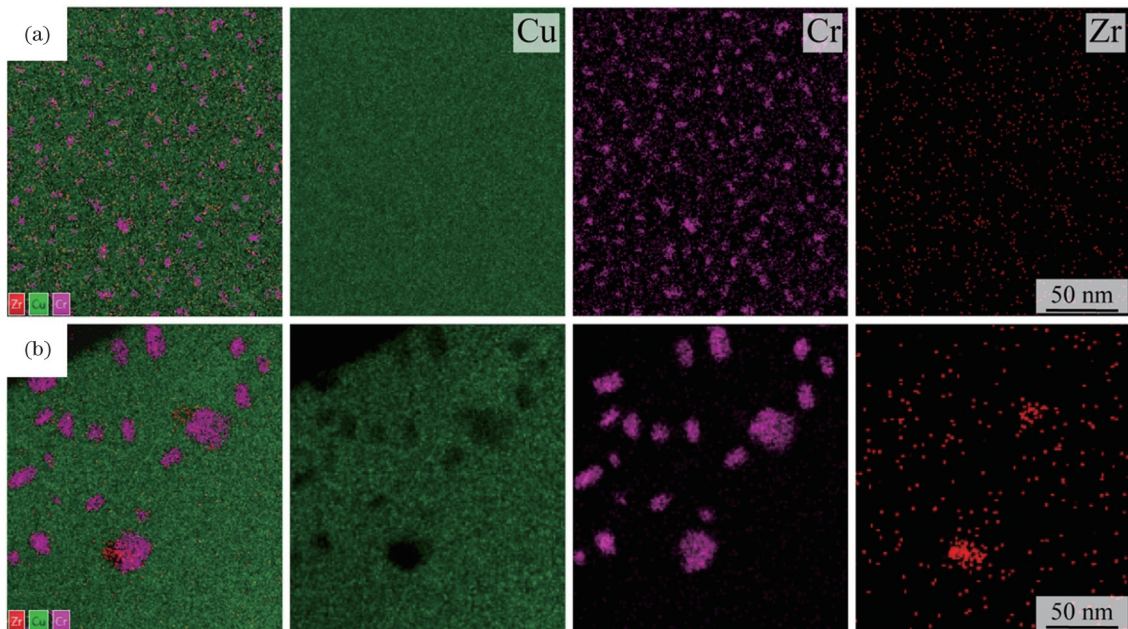


图 13 TEM-EDS 分析结果^[16]。(a) 480 °C 时效处理 4 h 试样的 Cr 沉淀物的分散分布；(b) 580 °C 时效处理 4 h 试样的聚集和生长的 Cr 和 Zr 沉淀物

Fig. 13 TEM-EDS analysis results^[16]. (a) Dispersed distribution of chromium precipitates in sample (480 °C aging treatment for 4 h); (b) aggregated and growing chromium and zirconium precipitates in sample (580 °C aging treatment for 4 h)

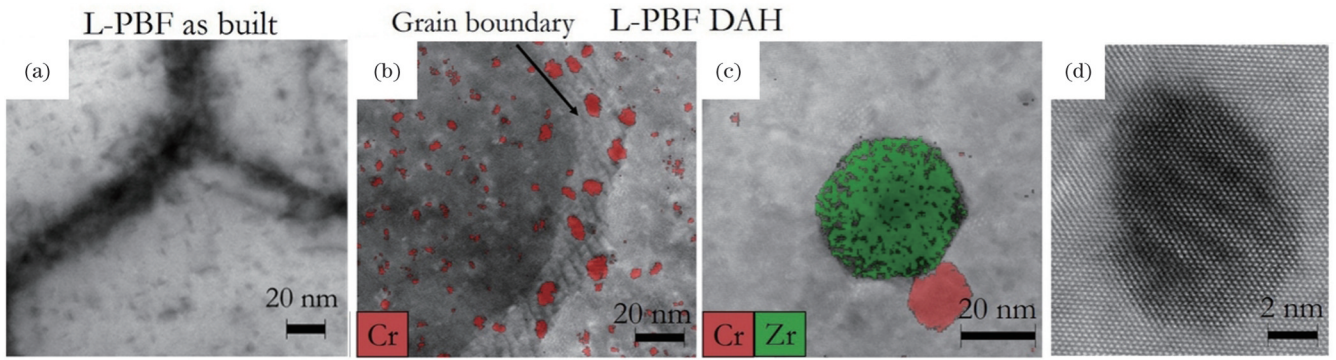


图 14 HAADF/STEM 与 Cr 和 Zr EDX 分析结果^[20]。(a)沉积态试样中未发现微纳米沉淀；(b)DAH 后检测到的 Cr 沉淀；(c)DAH 后在 Cr 沉淀旁出现的 Zr 沉淀；(d)纯 Cu 基质

Fig. 14 HAADF/STEM and Cr and Zr EDX analysis results^[20]. (a) No micro and nano-precipitates detected in the as-built samples; (b) Cr precipitates detected after DAH; (c) Zr precipitates appearing next to Cr precipitates after DAH; (d) substrate of pure Cu

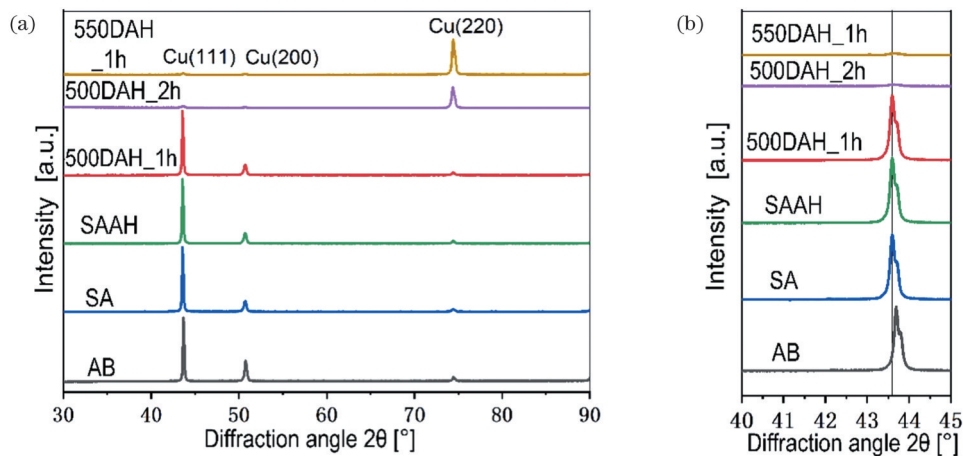


图 15 XRD 谱图^[25]。(a)沉积态 CuCrZr 和热处理 CuCrZr 试样；(b) 2θ 在 $40^\circ\sim 45^\circ$ 范围内的光谱放大图

Fig. 15 XRD patterns^[25]. (a) CuCrZr samples in the as-built state and CuCrZr samples with heat treatments; (b) enlarged spectra in the $40^\circ\sim 45^\circ$ 2θ range

下观察到 α -Cu 和 Cr 衍射峰,并且发现与 Tang 等现象:时效温度升高到 550°C 以上时,Cu 的晶粒取向发生明显变化, $\{200\}$ 和 $\{111\}$ 衍射峰强度降低, $\{220\}$ 衍射峰强度显著增加。

4 CuCrZr 合金的性能研究进展

Cu 及 Cu 合金不仅是力学材料,还是功能材料。新一代信息技术、先进轨道交通装备、航空航天装备、节能与新能源汽车等产业是我国重点发展的高新技术领域,而这些领域的关键基础材料之一是高性能的铜合金。此外,CuCrZr 系合金还是高速轨道交通接触线和超大规模集成电路引线框架的理想材料,这些应用都与其力学性能、导热性能和导电性能有着极大的联系^[62]。故本文分别对 CuCrZr 合金的力学、电学和热学性能进行讨论。

4.1 力学性能

表 3 统计了近年来的研究中热处理方法对 L-PBF 制备 CuCrZr 合金力学性能的影响,其中 SAAH 表示固溶退火+时效硬化。大多研究结果表明,在

热处理后使用绿激光制备的试样屈服强度及拉伸强度均高于使用近红外激光制备的试样^[24-25, 28]。大部分采用近红外激光制备的沉积态试样的力学性能较弱(屈服强度为 $175\sim 270$ MPa,极限拉伸强度为 $254\sim 347$ MPa,延展率为 $20.5\%\sim 42.4\%$)。在直接时效处理后,屈服强度($361\sim 527$ MPa)、极限拉伸强度($466\sim 585$ MPa)大幅增加,但是牺牲了延展率($5\%\sim 25\%$)。固溶退火+时效硬化处理对力学性能的增强效果有限(屈服强度为 $231\sim 253$ MPa,极限拉伸强度为 $322\sim 380$ MPa)。使用绿激光制备的沉积态试样的力学性能较强,Tang 等^[25]制备得到屈服强度为 400 MPa、极限拉伸强度为 447 MPa 的试样,但是其延展率较低,仅有 10% 。在直接时效硬化处理($500^\circ\text{C}\times 1$ h)后,试样的力学性能得到了全面提升,屈服强度、极限拉伸强度及延展率分别达到 487 MPa、 566 MPa 和 15% 。L-PBF 制备 CuCrZr 合金力学性能提升的最佳热处理方式是直接时效处理,优化处理条件为 500°C 左右处理 $1\sim 2$ h。

L-PBF 工艺的特性决定了微观组织的各向异性,进而决定了力学性能的各向异性。沿垂直方向的试样在热处理前后都有着比水平方向试样更高的显微硬度,但抗拉伸性能与之相反。因为柱状晶粒平行于垂

直方向生长,几乎没有横向晶界,在晶界阻力较小的情况下,位错更容易被激活并沿纵向移动而不会越过晶界,因此位错堆积引起的加工硬化不明显,导致抗拉强度相对较低^[63-64]。

表 3 热处理方法对力学性能的影响

Table 3 Effect of heat treatment methods on mechanical properties

Mass fraction of major alloying element / %		Yield strength / MPa	Ultimate tensile strength / MPa	Elongation / %	Heat treatment system	Ref.
Cr	Zr					
0.5-0.7	0.06-0.15	210.0	267.0	21.0	AB	Guan <i>et al.</i> ^[23] 2019
		405.0	490.0	12.5	DAH (500 °C×1 h)	
0.88	0.13	218.0±6.1	254.6±4.2	46.5±2.1	AB	Bai <i>et al.</i> ^[45] 2021
		131.0±1.0	254.9±4.5	41.4±2.0	ST (950 °C×0.5 h)	
		231.3±3.2	322.3±3.7	19.1±0.8	SAT (950 °C×0.5 h+ 480 °C×2 h)	
0.88	0.14	175.2	265.5	49.4	AB	Wang <i>et al.</i> ^[26] 2022
		502.5	612.0	21.8	DAH (480 °C×2 h)	
0.6-0.8	0.06-0.2	216.0	338.0	42.4	AB	Kuai <i>et al.</i> ^[28] 2022
0.5-0.7	0.06-0.15	400.0±11.0	447.0±13.0	10.0±3.0	AB	Tang <i>et al.</i> ^[25] 2022
		487.0±13.0	566.0±18.0	15.0±1.0	DAH (500 °C×1 h)	
0.6	0.15	213.0	262.0	32.0	AB	Yang <i>et al.</i> ^[16] 2023
		404.0	501.0	20.0	DA (480 °C×4 h)	
0.5-1.2	0.03-0.3	204.0±1.0	287.0±2.0	20.5±2.2	AB	Wallis <i>et al.</i> ^[24] 2019
		361.0±8.0	466.0±8.0	12.3±0.4	DAH (580 °C×5 h)	
		270.0±6.0	305.0±5.0	26.0±2.0	AB	
0.75	0.08	253.0±8.0	380.0±7.0	25.0±2.0	SAAH (980 °C×1 h+ 490 °C×6 h)	Salvan <i>et al.</i> ^[20] 2021
		527.0±3.0	585.0±1.0	14.0±1.0	DAH (490 °C×1 h)	
1.5	0.5	165.4±1.4	200.3±4.1	17.5±2.3	AB	Zeng <i>et al.</i> ^[57] 2019
		389.1±3.6	413.7±7.7	5.7±1.0	DAH (500 °C×2 h)	

L-PBF 制备的 CuCrZr 合金的凝固速度快,会产生高密度的位错和残余应力,为了提高合金的性能,在 L-PBF 加工后需要进行热处理^[65]。如表 3 所示,热处理之后,CuCrZr 合金的力学性能显著提高,这有两个主要原因:1) 位错密度和残余热应力在热处理过程中降低;2) 热处理期间产生纳米级的 Cr 和 Cu_xZr_y 颗粒,微纳米沉淀提高了合金的力学性能。合金中的高密度位错在热处理过程中会重新排列,位错强化对合金的影响在热处理后会降低^[32]。进一步对 4 种强化机制(晶界强化、位错强度强化、固溶强化和沉淀强化)的影响进行理论计算,发现沉淀强化对力学性能的影响最大^[16]。

如图 16 所示,Xie 等^[31]发现与沿水平方向的试样相比,沿垂直方向的试样在成形和时效处理后拉伸性能都更差。Zeng 等^[57]发现 L-PBF 制备 CuCrZr 合金的

拉伸性能各向异性,并得到与 Xie 等类似的结论,即沉积态试样在水平方向上的抗拉强度略高于沿垂直方向的抗拉强度,且具有更好的延展率。

在室温力学性能方面,Yang 等^[16]分别在 480 °C、530 °C 和 580 °C 温度下对试样进行了 4 h 的直接时效处理,结果显示,时效处理显著提升了屈服强度和极限拉伸强度,但是降低了延展率,且随着时效温度的升高,屈服强度和极限拉伸强度降低。Wang 等^[26]在 480 °C×2 h 的条件下直接时效硬化处理得到了力学性能极其优异的试样,该试样的屈服强度及极限拉伸强度分别达到 502.5 MPa 及 612.0 MPa,延展率也能达到 21.8%。时效处理的条件对于力学性能有着较大的影响,最佳的时效处理条件为 500 °C 左右处理 1~2 h。

在高温力学性能方面,Zeng 等^[57]研究了时效处理

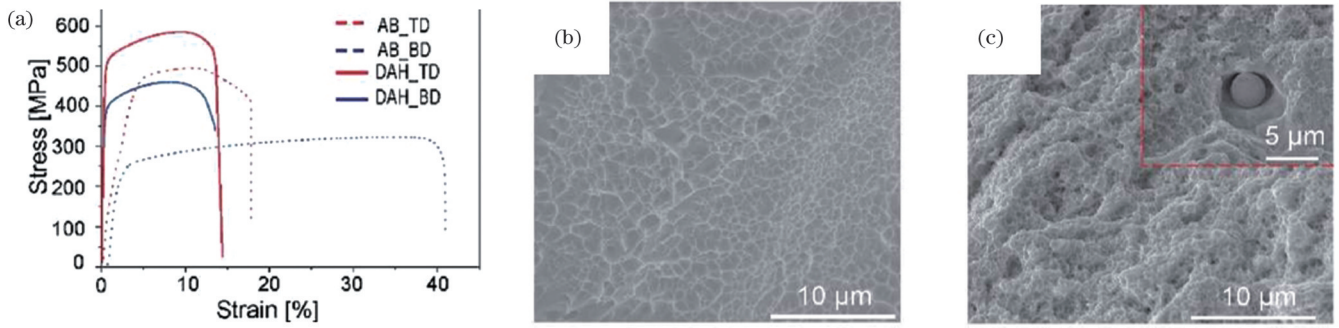


图 16 L-PBF 制造 CuCrZr 合金的力学行为^[31]。(a)水平、垂直构建方向上试样的应力与应变图；(b)沿水平方向的拉伸断裂面图；(c)沿垂直方向的拉伸断裂面图

Fig. 16 Mechanical behavior of L-PBF-built CuCrZr alloys^[31]. (a) Stress and strain plots of samples in horizontal and vertical building directions; (b) tensile fracture surface plots in horizontal building direction; (c) tensile fracture surface plots in vertical building direction

温度变化对 CuCrZr 合金拉伸性能的影响,分别在室温、204 °C 和 427 °C 下进行测试,所有经过热处理的试样都在空气中进行 2 h 的时效处理,拉伸实验的结果如

图 17 所示。同样可以看出:时效处理温度在 500 °C 附近,试样的拉伸性能最佳;随着处理温度升高,试样的力学性能下降。

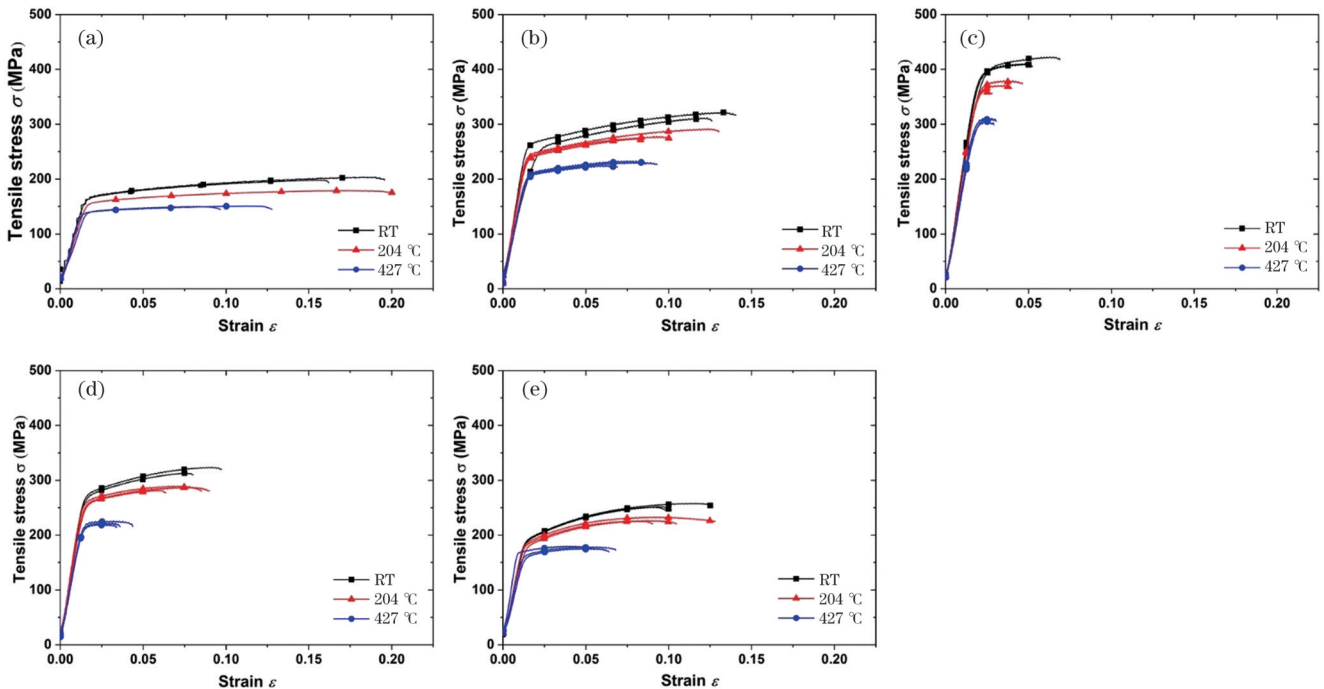


图 17 沿垂直方向试样在室温、204 °C、427 °C 下的拉伸实验结果^[57]。(a)AB 试样；(b) 420 °C 时效处理 2 h；(c) 500 °C 时效处理 2 h；(d) 575 °C 时效处理 2 h；(e) 650 °C 时效处理 2 h

Fig. 17 Tensile test results of samples along the build direction at room temperature, 204 °C, and 427 °C^[57]. (a) AB sample; (b) 420 °C aging treatment for 2 h; (c) 500 °C aging treatment for 2 h; (d) 575 °C aging treatment for 2 h; (e) 650 °C aging treatment for 2 h

4.2 导电性能

本文使用国际退火铜标准(% IACS)来对试样的导电性进行表征,纯 Cu 的电导率为 58 MS/m(100% IACS)^[30]。使用电阻率表征合金电导率,根据 Mattiessen 规则,CuCrZr 合金的电阻率可以表示为

$$\rho_t = \rho_0 + \rho_T + \rho_{SS} + \rho_{GB} + \rho_D + \rho_H + \rho_I, \quad (2)$$

式中: ρ_t 表示总电阻率; ρ_0 表示理想的纯金属电阻率; ρ_T 表示由温度影响而产生的电阻率; ρ_{SS} 、 ρ_{GB} 、 ρ_D 、 ρ_H 、 ρ_I 分别表示由固溶体原子、晶界、位错、成形缺陷、杂质影响

而产生的电阻率。其中,相同的成形质量及环境温度下,固溶体原子对电阻率的影响最大^[30]。

表 4 所示为热处理方法对电导率的影响,沉积态 CuCrZr 合金试样的电导率在 15.6% IACS~31.0% IACS 范围,电导率与致密度呈正相关关系,但是致密度对电导率的提升有限。在热处理后 CuCrZr 合金试样的电导率提高到 83% IACS~97% IACS。对于 L-PBF 制备 CuCrZr 合金电学性能提升的最佳热处理方式是固溶退火+时效硬化处理,优化处理条件分别

为 950 °C~1000 °C×1 h 及 500 °C 左右×1~3 h。直接时效处理后也能得到较高电导率的试样,不过在同一研究中,最佳力学性能与最佳电学性能的直接时效处理温度条件不同^[20,24-25]。与纯 Cu 和传统铸造的 CuCrZr 合金相比,大部分 L-PBF 制备的沉积态 CuCrZr 合金的电导率较低,这是因为在 L-PBF 制备试

样的过程中,快速凝固使 Cr 和 Zr 元素在铜基体中形成大量过饱和固溶体,基体中的固溶原子导致晶粒的晶格畸变,对自由电子散射作用的加强显著降低了试样的电导率^[16]。电导率同样存在各向异性,水平方向试样的电导率低于垂直方向试样电导率的原因主要是水平方向试样中晶格畸变的程度更高^[66]。

表 4 热处理方法对电导率的影响

Table 4 Effect of heat treatment method on electrical conductivity

Mass fraction of major alloying elements / %		Density / %	Conductivity / (% IACS)	Heat treatment system	Ref.
Cr	Zr				
0.88	0.14	96.6–98.3	22.2	AB	Wang <i>et al.</i> ^[26] , 2022
0.5–1.5	0.05–0.25	99.3	21.0–26.0	AB	Ou <i>et al.</i> ^[30] , 2022
			91.20±0.49	ST (1000 °C×2 h)	
0.60	0.15	99.9	28.0	AB	Yang <i>et al.</i> ^[16] , 2023
			97.0	DA (580 °C×4 h)	
0.5–1.2	0.03–0.3	99.4	24.6	AB	Salvan <i>et al.</i> ^[20] , 2021
			88.1	SAAH (980 °C×1 h+490 °C×3 h)	
0.50–0.70	0.06–0.15	98.0	30.0±1.0	AB	Tang <i>et al.</i> ^[25] , 2022
			84.0±1.0	SAAH (960 °C×1 h+500 °C×1 h)	
0.50–0.70	0.06–0.15	–	83.0±1.0	DAH (550 °C×1 h)	Xie <i>et al.</i> ^[31] , 2023
			30.0	AB	
			64.0	DAH (500 °C×1 h)	

在沉积态下,欧远辉等^[30]发现电导率与致密度呈正相关关系,但是所有试样的电导率都分布在 21.0% IACS~26.0% IACS,如图 18 所示。在热处理条件下,如图 19(a)所示,Tang 等^[25]对沉积态试样进行热处理后得到热处理对电导率的影响规律。热处理大幅提高了 CuCrZr 合金的导电性能,其中固溶退火+时效硬化处理后试样的导电性能最佳,在时效处理中

温度对试样的电导率有着较大影响。Yang 等^[16]也观察到相同的规律[图 19(b)],时效处理温度最高(580 °C×4 h)时试样的导电性能最佳(97% IACS)。Salavn 等^[20]也发现固溶退火+时效硬化处理后试样的导电性能得到极大提升,接近铸造制备的 CuCrZr 合金[图 19(c)],这说明 L-PBF 制备 CuCrZr 合金在热处理后同样能得到导电性能很好的试样。综上,固

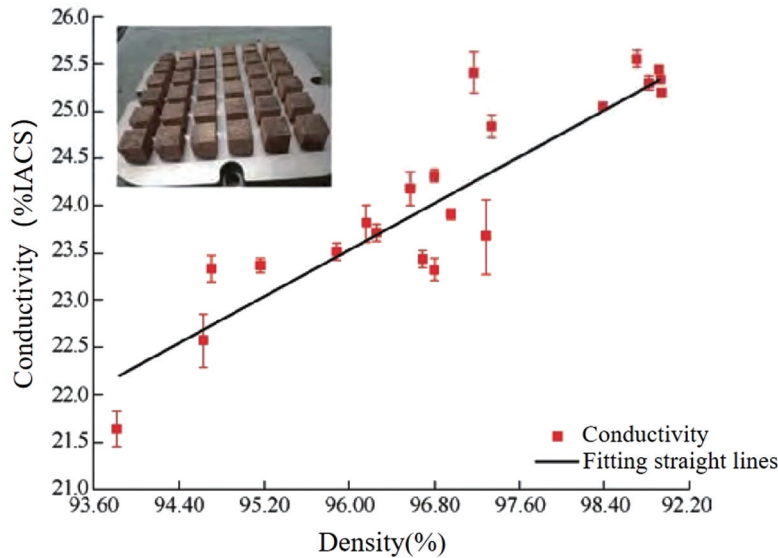


图 18 致密度与电导率的关系^[30]

Fig. 18 Relationship between density and electrical conductivity^[30]

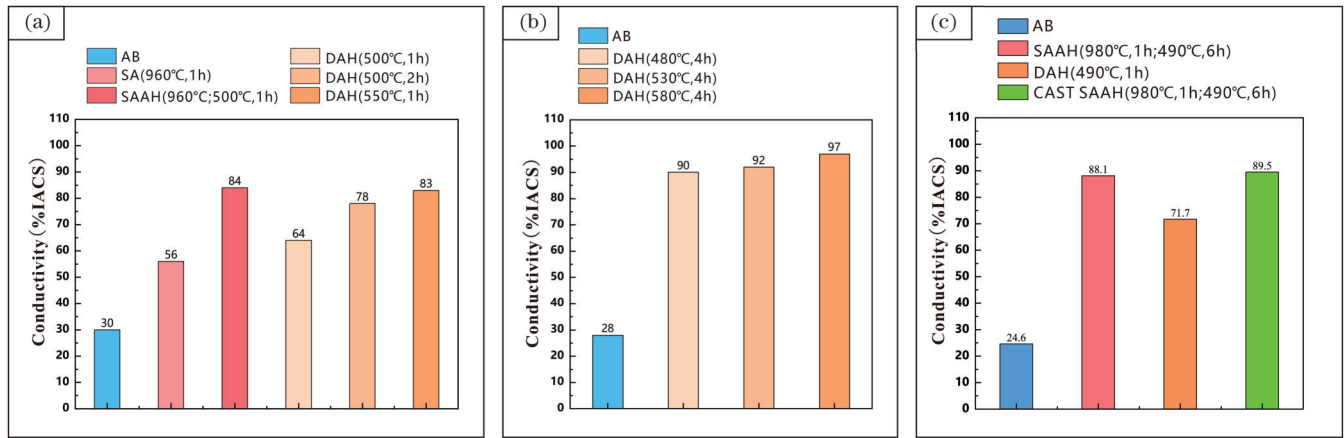


图 19 热处理对导电性能的影响。(a) Tang 等^[25]对热处理影响导电性能的研究；(b) Yang 等^[16]对热处理影响导电性能的研究；(c) Salvan 等^[20]对热处理影响导电性能的研究

Fig. 19 Effect of heat treatment on electrical conductivity. (a) Tang *et al.*^[25] on heat treatment affecting electrical conductivity; (b) Yang *et al.*^[16] on heat treatment affecting electrical conductivity; (c) Salvan *et al.*^[20] on heat treatment affecting electrical conductivity

溶退火+时效硬化处理能得到比直接时效处理更优异导电性能的试样。

4.3 导热性能

Xie 等^[31]发现 L-PBF 制备的 CuCrZr 合金在导热性能方面同样具有明显的各向异性,沿垂直方向的试样的热性能弱于沿水平方向的试样,如图 20 所示。随着处理温度的升高,Cu 基体中固溶的 Cr 及 Zr 原子的沉淀相数量逐渐增加,从而降低了热阻,增加了热导率^[16]。如表 5 所示,L-PBF 制备 CuCrZr 合金热学性能

提升的最佳热处理方式是 SAAH 固溶退火+时效硬化处理,处理条件分别为 950~1000 °C×1 h 及 500 °C 左右×1~3 h,直接时效硬化处理也能得到较高电导率的试样,并且最佳热学性能与最佳电学性能所需的热处理条件相同。Tang 等^[25]在固溶退火+时效硬化处理和直接时效硬化处理后分别得到 (350±4) W/(m·K) 及 (346±4) W/(m·K) 的热导率。Yang 等^[16]采用直接时效处理,将试样热导率提高到 313 W/(m·K),该试样同时也是该研究中电导率最优的试样。

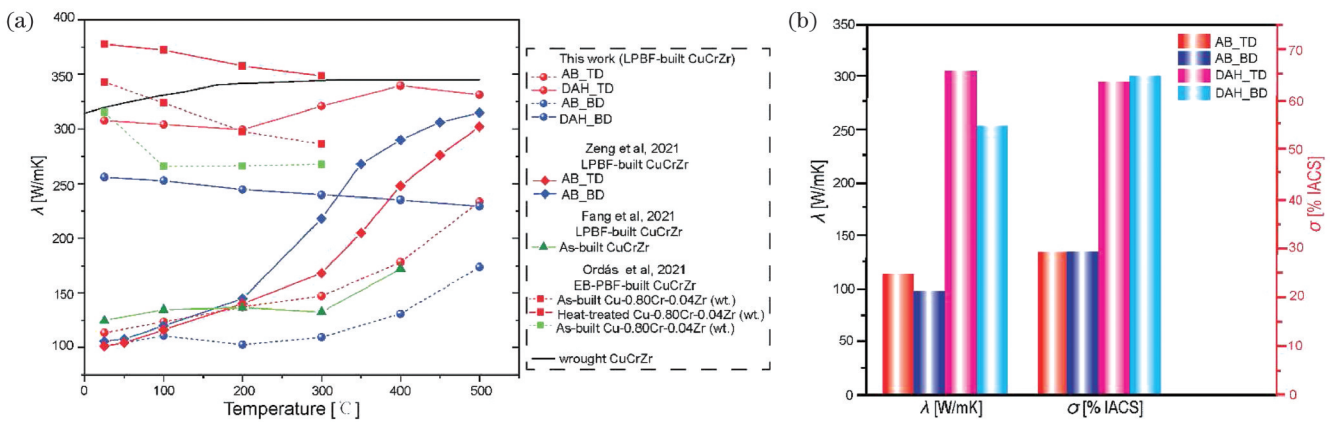


图 20 L-PBF 制造的 CuCrZr 合金的导热和导电性能^[31]。(a) CuCrZr 试样的热导率随温度的变化；(b) 时效温度对试样热导率的影响

与电导率的变化相同,由于 L-PBF 制备试样时冷却速率高,因此试样的铜基质中具有大量过饱和 Cr、Zr 原子,其对自由电子的强散射作用降低了沉积态合金的热导率,合金热导率与致密度同样呈正相关关系,这导致 L-PBF 制备的 CuCrZr 合金热导率较差^[50]。热处理对热导率的影响显著,直接时效处理对微观组织的影响很小,通过抑制沉淀的产生来提升导热性能,处理时间的增加和处理温度的升高都会使热导率增大。

固溶退火+时效硬化处理能获得最佳热导率的试样,一方面是因为固溶处理会降低位错密度,而延长处理时间和提升处理温度都会进一步减少位错密度,另一方面是因为固溶退火+时效硬化处理在晶粒内形成由 Cr 相和富 Zr 相组成的纳米级细小分散沉淀物,核-壳结构表明,富 Cr 核被富 Zr 壳包围,固溶体发生分解和元素分区,形成带有细小沉淀物的近纯 Cu 基体,使得 CuCrZr 合金的热导率提高^[24]。

表 5 热处理制度对热导率的影响

Table 5 Effect of heat treatment method on thermal conductivity

Mass fraction of major alloying elements / %		Density / %	Thermal conductivity / [W·(m·K) ⁻¹]	Heat treatment system	Ref.
Cr	Zr				
			125.0±4.0	AB	
0.5-0.7	0.06-0.15	98.0	346.0±4.0	DAH (550 °C×1 h)	Tang <i>et al.</i> ^[25] , 2022
			350.0±4.0	SAAH (960 °C×1 h+500 °C×1 h)	
0.6	0.15	99.9	102.0	AB	Yang <i>et al.</i> ^[16] , 2023
			313.0	DA (580 °C×4 h)	
0.5-1.2	0.03-0.3	99.9	100.0±2.0	AB	Wallis <i>et al.</i> ^[24] , 2019
			297.0±6.0	SAAH (950 °C×0.25 h+450 °C×2 h)	
			307.0	DAH (550 °C×1 h)	
0.5-0.7	0.06-0.15	-		parallel horizontal direction	Xie <i>et al.</i> ^[31] , 2023
			255.0	DAH (550 °C×1 h)	
				parallel vertical direction	

5 总结和展望

综述了 L-PBF 制备 CuCrZr 合金的成形行为(工艺参数、激光波长)、微观组织(沉积态、热处理)和综合性能(力学、电学、热学)的研究进展,主要结论如下:

1) 由于 CuCrZr 合金对绿激光的吸收率显著高于对近红外激光的吸收率,合金粉末对激光的吸收率与波长成反比,吸收率在激光波长超过 550 nm 后急剧降低,导致近红外激光的 E_A (20~200 J/mm³) 普遍比绿激光的 E_A (100~500 J/mm³) 低。与近红外激光相比,绿激光制备 CuCrZr 合金的致密度波动范围更小 (96.5%~98.5% vs. 95.5%~99.9%), 但整体致密度偏低,说明绿激光的工艺参数仍有优化空间。孔隙、裂纹及未熔粉末是 LAM 制备 CuCrZr 合金中最常见并且较难遏制的缺陷。

2) 固溶处理能使合金的熔池边界消失并改变晶粒形态,时效处理会产生沉淀进而提升合金的力学性能。L-PBF 制备 CuCrZr 合金会在基体固溶大量的过饱和 Cr、Zr 原子,直接时效处理后在基体析出,处理后 CuCrZr 合金的主要沉淀物为 Cr₃Cu₂Zr₃ 和 Cr₂Zr, 这些细小的微纳米沉淀物可以强化合金的力学性能,随着处理温度的增加,沉淀的分布方式也会改变(从均匀分布到部分集中),并且 500 °C×2 h 或 550 °C×1 h 的时效处理会使得 CuCrZr 合金 {111}、{200} 晶面的取向变弱, {220} 晶面的取向变强。

3) 沉积态 CuCrZr 合金的力学性能较差(屈服强度为 175.2~400.0 MPa, 极限拉伸强度为 254.6~447.0 MPa, 延展率为 10.0%~49.4%), 其中力学性能最优的沉积态 CuCrZr 合金是使用绿激光制备的。对于试样力学性能的提升效果最好的热处理方法是直接时效处理,处理条件为 500 °C 左右×1~2 h。经时效处理后的 CuCrZr 合金力学性能得到大幅增强(屈服强度为

361.0~527.0 MPa, 极限拉伸强度为 466.0~612.0 MPa, 延展率为 12.3%~21.8%), 时效处理产生沉淀物并降低位错密度和热残余应力,使得 CuCrZr 合金的力学性能得到极大的提升。

4) 沉积态 CuCrZr 合金的电导率在 21% IACS~30.0% IACS 范围内,热导率在 100.0~307.0 W/(m·K) 范围内。试样中基质存在大量由过饱和 Cr、Zr 原子导致的晶格畸变,这些晶格畸变加强了对自由电子的散射作用,从而使得试样的电导率和热导率降低。对于电导率和热导率提升最好的热处理工艺都是固溶退火+时效硬化,处理条件为 950~1000 °C×1 h 及 500 °C 左右×1~3 h,处理后电导率和热导率分别达到 84.0% IACS~88.1% IACS 和 297.0~350.0 W/(m·K), 固溶退火+时效硬化处理降低了位错密度和残余应力并产生沉淀物,从而提升了试样的电导率和热导率。

目前尚未完全探明绿激光/近红外激光对 CuCrZr 合金成形行为的影响规律,尚未厘清 LAM 制备 CuCrZr 合金的力学、电学及热学性能的调控机理。针对上述现状,未来对 LAM 制备 CuCrZr 合金的研究将会集中在以下几个方面:

1) 优化绿激光制备 CuCrZr 合金的工艺参数,分析其微观组织与近红外激光制备试样的异同,探究其性能差异的原因,从而获得致密度更高、性能更好的 CuCrZr 合金。探索使用混合激光(如蓝/绿激光+近红外激光)制备 CuCrZr 合金。

2) 传统的体积能量密度对于工艺参数的优化研究还有着较大的局限性,其未考虑材料的特性,目前迫切需要一种能综合考虑材料特性与 LAM 工艺参数的方法。

3) 探索抗拉强度、延展率之间的最佳平衡点,对热学、电学性能进行综合研究,优化热处理工艺,综合提升 LAM 制备 CuCrZr 合金的力学、电学及热学性能。

4) 已有研究人员通过 EB-PBF 工艺制备得到等轴晶粒的铜合金(镍铝青铜合金, C63000), 该铜合金表现出力学性能各向同性的特性, 并具有高强度和高延展率。未来同样有希望制备出具有等轴晶粒结构的 CuCrZr 合金。

参 考 文 献

- [1] 顾冬冬, 张红梅, 陈洪宇, 等. 航空航天高性能金属材料构件激光增材制造[J]. 中国激光, 2020, 47(5): 0500002.
Gu D D, Zhang H M, Chen H Y, et al. Laser additive manufacturing of high-performance metallic aerospace components [J]. Chinese Journal of Lasers, 2020, 47(5): 0500002.
- [2] MacDonald E, Wicker R. Multiprocess 3D printing for increasing component functionality[J]. Science, 2016, 353(6307): aaf2093.
- [3] Biffi C A, Fiochi J, Boldrini S, et al. CuCrZr alloy manufactured by LPBF process: correlation between microstructure, mechanical and thermal properties[J/OL]. Lasers in Manufacturing and Materials Processing: 1-11[2024-01-18]. <https://link.springer.com/article/10.1007/s40516-023-00240-7#citeas>.
- [4] 张阳军, 陈英. 金属材料增材制造技术的应用研究进展[J]. 粉末冶金工业, 2018, 28(1): 63-67.
Zhang Y J, Chen Y. Research on the application of metal additive manufacturing technology[J]. Powder Metallurgy Industry, 2018, 28(1): 63-67.
- [5] 邓怀波, 陈玉华, 陈伟, 等. 铜合金增材制造技术研究进展[J]. 精密成形工程, 2018, 10(5): 95-101.
Deng H B, Chen Y H, Chen W, et al. Research progress in additive manufacturing technology of copper alloy[J]. Journal of Netshape Forming Engineering, 2018, 10(5): 95-101.
- [6] Popovich A, Sufiarov V, Polozov I, et al. Microstructure and mechanical properties of additive manufactured copper alloy[J]. Materials Letters, 2016, 179: 38-41.
- [7] 王迪, 卫洋, 田印仞, 等. 应用于增材制造的纯铜/铜合金材料研究前沿进展[J]. 工业技术创新, 2023, 10(3): 9-23.
Wang D, Wei Y, Tian Y Q, et al. Frontiers of research on pure copper/copper alloy materials for additive manufacturing[J]. Industrial Technology Innovation, 2023, 10(3): 9-23.
- [8] Murali D S, Kumar S, Choudhary R J, et al. Synthesis of Cu₂O from CuO thin films: optical and electrical properties[J]. AIP Advances, 2015, 5(4): 047143.
- [9] Jiang Q, Zhang P L, Yu Z S, et al. A review on additive manufacturing of pure copper[J]. Coatings, 2021, 11(6): 740.
- [10] Yang C, Zhao Y J, Kang L M, et al. High-strength silicon brass manufactured by selective laser melting[J]. Materials Letters, 2018, 210: 169-172.
- [11] Scudino S, Unterdörfer C, Prashanth K G, et al. Additive manufacturing of Cu-10Sn bronze[J]. Materials Letters, 2015, 156: 202-204.
- [12] Wang J B, Zhou X L, Li J H, et al. A comparative study of Cu-15Ni-8Sn alloy prepared by L-DED and L-PBF: microstructure and properties[J]. Materials Science and Engineering A, 2022, 840: 142934.
- [13] 李宗武. Cu-Cr 系合金组织与高温性能研究[D]. 北京: 北京有色金属研究总院, 2019.
Li Z W. Study on microstructure and high temperature properties of Cu-Cr alloys[D]. Beijing: Beijing General Research Institute for Nonferrous Metals, 2019.
- [14] 胡号旗, 许赫, 杨丽景, 等. 高强高导铜铬锆合金的最新研究进展[J]. 材料导报, 2018, 32(3): 453-460.
Hu H Q, Xu C, Yang L J, et al. Recent advances in the research of high-strength and high-conductivity CuCrZr alloy[J]. Materials Review, 2018, 32(3): 453-460.
- [15] Zhang X X, Yuan Y L, Zhao S Q, et al. Microstructure stability, softening temperature and strengthening mechanism of pure copper, CuCrZr and Cu-Al₂O₃ up to 1000 °C[J]. Nuclear Materials and Energy, 2022, 30: 101123.
- [16] Yang X, Qi Y, Zhang W Q, et al. Laser powder bed fusion of C18150 copper alloy with excellent comprehensive properties[J]. Materials Science and Engineering: A, 2023, 862: 144512.
- [17] Kalinin G M, Ivanov A D, Obushev A N, et al. Ageing effect on the properties of CuCrZr alloy used for the ITER HNF components [J]. Journal of Nuclear Materials, 2007, 367/368/369/370: 920-924.
- [18] 朱卉平, 刘旭东, 陈嘉威, 等. 聚变堆用 CuCrZr 合金腐蚀模型研究及实验验证[J]. 核技术, 2020, 43(11): 80-86.
Zhu H P, Liu X D, Chen J W, et al. Study on corrosion model and experimental verification of CuCrZr alloy for fusion reactor[J]. Nuclear Techniques, 2020, 43(11): 80-86.
- [19] Li R G, Guo E Y, Chen Z N, et al. Optimization of the balance between high strength and high electrical conductivity in CuCrZr alloys through two-step cryorolling and aging[J]. Journal of Alloys and Compounds, 2019, 771: 1044-1051.
- [20] Salván C, Briottet L, Baffie T, et al. CuCrZr alloy produced by laser powder bed fusion: microstructure, nanoscale strengthening mechanisms, electrical and mechanical properties[J]. Materials Science and Engineering A, 2021, 826: 141915.
- [21] Zhang Z Y, Sun L X, Tao N R. Nanostructures and nanoprecipitates induce high strength and high electrical conductivity in a CuCrZr alloy[J]. Journal of Materials Science & Technology, 2020, 48: 18-22.
- [22] Ordás N, Portolés L, Azpeleta M, et al. Development of CuCrZr via electron beam powder bed fusion (EB-PBF) [J]. Journal of Nuclear Materials, 2021, 548: 152841.
- [23] Guan P F, Chen X H, Liu P, et al. Effect of selective laser melting process parameters and aging heat treatment on properties of CuCrZr alloy[J]. Materials Research Express, 2019, 6(11): 1165c1.
- [24] Wallis C, Buchmayr B. Effect of heat treatments on microstructure and properties of CuCrZr produced by laser-powder bed fusion[J]. Materials Science and Engineering A, 2019, 744: 215-223.
- [25] Tang X P, Chen X H, Sun F J, et al. A study on the mechanical and electrical properties of high-strength CuCrZr alloy fabricated using laser powder bed fusion[J]. Journal of Alloys and Compounds, 2022, 924: 166627.
- [26] Wang Q J, Zhang Y F, Wang K S, et al. Effect of process parameters and heat treatment on the microstructure and properties of CuCrZr alloy by selective laser melting[J]. Materials Science and Engineering A, 2022, 857: 144054.
- [27] 国家市场监督管理总局, 国家标准化管理委员会. 加工铜及铜合金牌号和化学成分: GB/T 5231—2022[S]. 北京: 中国标准出版社, 2022.
State Administration for Market Regulation, Standardization Administration of the People's Republic of China. Designation and chemical composition of wrought copper and copper alloys: GB/T 5231—2022[S]. Beijing: Standards Press of China, 2022.
- [28] Kuai Z Z, Li Z H, Liu B, et al. Effect of heat treatment on CuCrZr alloy fabricated by selective laser melting: microstructure evolution, mechanical properties and fracture mechanism[J]. Journal of Materials Research and Technology, 2023, 23: 2658-2671.
- [29] Zeng C Y, Wen H, Bernard B C, et al. Effect of temperature history on thermal properties of additively manufactured C-18150 alloy samples[J]. Manufacturing Letters, 2021, 28: 25-29.
- [30] 欧远辉, 王迪, 刘林青, 等. 激光选区熔化成形 CuCrZr 合金电导率提升机理研究[J]. 机械工程学报, 2022, 58(17): 297-308.
Ou Y H, Wang D, Liu L Q, et al. Mechanisms of electrical conductivity improvement of CuCrZr alloy produced by selective laser melting[J]. Journal of Mechanical Engineering, 2022, 58(17): 297-308.
- [31] Xie H F, Tang X P, Chen X H, et al. The effect of build orientations on mechanical and thermal properties on CuCrZr alloys fabricated by laser powder bed fusion[J]. Journal of Materials Research and Technology, 2023, 23: 3322-3336.

- [32] Tang X P, Chen X H, Sun F J, et al. The current state of CuCrZr and CuCrNb alloys manufactured by additive manufacturing: a review[J]. *Materials & Design*, 2022, 224: 111419.
- [33] Cao L C, Li J C, Hu J X, et al. Optimization of surface roughness and dimensional accuracy in LPBF additive manufacturing[J]. *Optics & Laser Technology*, 2021, 142: 107246.
- [34] 周吉强, 黄玉山, 佟鑫, 等. CuCrZr 合金选区激光熔化成形工艺与力学性能研究[J]. *应用激光*, 2022, 42(3): 43-52.
Zhou J Q, Huang Y S, Tong X, et al. Process and mechanical properties of CuCrZr alloy fabricated by selective laser melting[J]. *Applied Laser*, 2022, 42(3): 43-52.
- [35] Kuai Z Z, Li Z H, Liu B, et al. Selective laser melting of CuCrZr alloy: processing optimisation, microstructure and mechanical properties[J]. *Journal of Materials Research and Technology*, 2022, 19: 4915-4931.
- [36] Bertoli U S, Wolfer A J, Matthews M J, et al. On the limitations of volumetric energy density as a design parameter for selective laser melting[J]. *Materials & Design*, 2017, 113: 331-340.
- [37] Ma Z B, Zhang S H, Gao C F, et al. The influence of structural design on the dimensional accuracy of CuCrZr alloy produced by laser powder bed fusion[J]. *Sustainability*, 2022, 14(21): 14639.
- [38] Wang Q J, Shao H J, Zhang X, et al. Study of thermal behavior and microstructure formation mechanism of CuCrZr alloy melted by laser powder bed fusion[J]. *Materials Characterization*, 2023, 198: 112721.
- [39] Ma Z B, Zhang K F, Ren Z H, et al. Selective laser melting of Cu-Cr-Zr copper alloy: parameter optimization, microstructure and mechanical properties[J]. *Journal of Alloys and Compounds*, 2020, 828: 154350.
- [40] Bacchewar P B, Singhal S K, Pandey P M. Statistical modelling and optimization of surface roughness in the selective laser sintering process[J]. *Proceedings of the Institution of Mechanical Engineers, Part B: Journal of Engineering Manufacture*, 2007, 221(1): 35-52.
- [41] Brandau B, Da Silva A, Wilsnack C, et al. Absorbance study of powder conditions for laser additive manufacturing[J]. *Materials & Design*, 2022, 216: 110591.
- [42] Lassègue P, Salvan C, De Vito E, et al. Laser powder bed fusion (L-PBF) of Cu and CuCrZr parts: influence of an absorptive physical vapor deposition (PVD) coating on the printing process[J]. *Additive Manufacturing*, 2021, 39: 101888.
- [43] Hummel M, Kulkens M, Schöler C, et al. *In situ* X-ray tomography investigations on laser welding of copper with 515 and 1030 nm laser beam sources[J]. *Journal of Manufacturing Processes*, 2021, 67: 170-176.
- [44] Fu J, Li H, Song X, et al. Multi-scale defects in powder-based additively manufactured metals and alloys[J]. *Journal of Materials Science & Technology*, 2022, 122: 165-199.
- [45] Bai Y C, Zhao C L, Zhang Y, et al. Additively manufactured CuCrZr alloy: microstructure, mechanical properties and machinability[J]. *Materials Science and Engineering A*, 2021, 819: 141528.
- [46] Li R D, Liu J H, Shi Y S, et al. Balling behavior of stainless steel and nickel powder during selective laser melting process[J]. *The International Journal of Advanced Manufacturing Technology*, 2012, 59(9): 1025-1035.
- [47] 石岩, 魏登松. 激光粉末床熔融增材制造未熔合气孔缺陷形成机理研究[J]. *中国激光*, 2023, 50(20): 2002303.
Shi Y, Wei D S. Lack-of-fusion porosity defects formation mechanism in laser powder bed fusion additive manufacturing[J]. *Chinese Journal of Lasers*, 2023, 50(20): 2002303.
- [48] 殷杰, 郝亮, 杨亮亮, 等. 激光选区熔化增材制造中金属蒸气与飞溅相互作用研究[J]. *中国激光*, 2022, 49(14): 1402202.
Yin J, Hao L, Yang L L, et al. Investigation of interaction between vapor plume and spatter during selective laser melting additive manufacturing[J]. *Chinese Journal of Lasers*, 2022, 49(14): 1402202.
- [49] 李军, 刘婷婷, 廖文和, 等. 激光选区熔化 GH3536 高温合金成形特征与缺陷研究[J]. *中国激光*, 2023, 50(12): 1202302.
Li J, Liu T T, Liao W H, et al. Forming characteristics and defects of GH3536 superalloy by selective laser melting[J]. *Chinese Journal of Lasers*, 2023, 50(12): 1202302.
- [50] Fang X Y, Xia W S, Wei Q S, et al. Preparation of Cu-Cr-Zr alloy by laser powder bed fusion: parameter optimization, microstructure, mechanical and thermal properties for microelectronic applications[J]. *Metals*, 2021, 11(9): 1410.
- [51] Tang Y T, Panwisawas C, Ghossoub J N, et al. Alloys-by-design: application to new superalloys for additive manufacturing[J]. *Acta Materialia*, 2021, 202: 417-436.
- [52] Thijs L, Verhaeghe F, Craeghs T, et al. A study of the microstructural evolution during selective laser melting of Ti-6Al-4V[J]. *Acta Materialia*, 2010, 58(9): 3303-3312.
- [53] Chauvet E, Kontis P, Jäggle E A, et al. Hot cracking mechanism affecting a non-weldable Ni-based superalloy produced by selective electron beam melting[J]. *Acta Materialia*, 2018, 142: 82-94.
- [54] King W E, Barth H D, Castillo V M, et al. Observation of keyhole-mode laser melting in laser powder-bed fusion additive manufacturing[J]. *Journal of Materials Processing Technology*, 2014, 214(12): 2915-2925.
- [55] Xiong W, Hao L, Peijs T, et al. Simultaneous strength and ductility enhancements of high thermal conductive Ag_{7.5}Cu alloy by selective laser melting[J]. *Scientific Reports*, 2022, 12: 4250.
- [56] Vikram R J, Kollo L, Prashanth K G, et al. Investigating the structure, microstructure, and texture in selective laser-melted sterling silver 925[J]. *Metallurgical and Materials Transactions A*, 2021, 52(12): 5329-5341.
- [57] Zeng C Y, Wen H, Bernard B C, et al. Tensile properties of additively manufactured C-18150 copper alloys[J]. *Metals and Materials International*, 2022, 28(1): 168-180.
- [58] Andersson J O, Helander T, Höglund L, et al. Thermo-Calc & DICTRA, computational tools for materials science[J]. *Calphad*, 2002, 26(2): 273-312.
- [59] Yang Y H, Lei Q, Zhang P, et al. Stabilization of L1₂ structured Cr₃Cu precipitates in a Cu-4.06Cr-1.25Nb alloy with high high-temperature strength[J]. *Materials Research Letters*, 2022, 10(4): 257-263.
- [60] Zhang S S, Zhu H H, Zhang L, et al. Microstructure and properties of high strength and high conductivity Cu-Cr alloy components fabricated by high power selective laser melting[J]. *Materials Letters*, 2019, 237: 306-309.
- [61] Zhang S S, Zhu H H, Zhang L, et al. Microstructure and properties in QCr_{0.8} alloy produced by selective laser melting with different heat treatment[J]. *Journal of Alloys and Compounds*, 2019, 800: 286-293.
- [62] 姜业欣, 娄花芬, 解浩峰, 等. 先进铜合金材料发展现状与展望[J]. *中国工程科学*, 2020, 22(5): 84-92.
Jiang Y X, Lou H F, Xie H F, et al. Development status and prospects of advanced copper alloy[J]. *Strategic Study of CAE*, 2020, 22(5): 84-92.
- [63] Gao K W, Liu M Y, Zou F L, et al. Characterization of microstructure evolution after severe plastic deformation of pure copper with continuous columnar crystals[J]. *Materials Science and Engineering A*, 2010, 527(18/19): 4750-4757.
- [64] Guschlbauer R, Burkhardt A K, Fu Z W, et al. Effect of the oxygen content of pure copper powder on selective electron beam melting[J]. *Materials Science and Engineering: A*, 2020, 779: 139106.
- [65] Ma G Y, Wu S N, Wang R Z, et al. Microstructure evaluation and resultant mechanical properties of laser-arc hybrid additive manufactured Cu-Cr-Zr alloy[J]. *Journal of Alloys and Compounds*, 2022, 912: 165044.
- [66] Hu Z P, Yang Z W, Du Z F, et al. Effect of scanning strategy on the anisotropy in microstructure and properties of Cu-Cr-Zr alloy manufactured by laser powder bed fusion[J]. *Journal of Alloys and Compounds*, 2022, 920: 165957.

Recent Progress in Laser Additive Manufacturing Using Copper-Chromium-Zirconium Alloys: Formation, Microstructure, and Comprehensive Properties (Invited)

Chen Xingyu^{1,2}, Li Hao^{1,2}, Chen Qiaoyu^{1,2}, Xu Haisheng³, Xie Fanxuan^{1,2}, Li Zheng^{1,2},
Huang Tianye⁴, Guan Kai⁵, Yin Zuowei^{1,2}, Hao Liang^{1,2}, Yin Jie^{1,2*}

¹*Gemological Institute, China University of Geosciences, Wuhan 430074, Hubei, China;*

²*Advanced Manufacturing Research Institute, China University of Geosciences, Wuhan 430074, Hubei, China;*

³*Hubei Sanjiang Aerospace Jiangbei Machinery Engineering Co., Ltd., Xiaogan 432000, Hubei, China;*

⁴*School of Mechanical Engineering and Electronic Information, China University of Geosciences, Wuhan 430074, Hubei, China;*

⁵*TSC Laser Technology Development (Beijing) Co., Ltd., Beijing 102200, China*

Abstract

Significance Laser additive manufacturing (LAM) is renowned for its exceptional accuracy and the ability to produce complex components with intricate geometries, making it widely used across various industries. The LAM technology primarily encompasses two techniques: laser-directed energy deposition (LP-DED) and laser powder bed fusion (L-PBF). Among these, L-PBF is witnessing rapid advancements and gaining popularity in both scientific research and industrial applications.

Copper and its alloys are pivotal functional materials. They act as crucial strategic reserves for the country, with a significant position within the national economy. Nevertheless, the exceptional thermal conductivity and high NIR reflectivity exhibited by copper and its alloys present notable challenges for LAM in relation to their effective processing and shaping. However, copper and its alloys have excellent electrical and thermal conductivities, along with exceptional mechanical properties. Because of the growing call for intricate functional copper and copper alloy components, the LAM of copper and copper alloy parts has become a research hotspot in recent years.

CuCrZr is a copper-based precipitation hardening alloy. The addition of chromium significantly enhances its mechanical properties when compared to pure copper. Meanwhile, the presence of zirconium effectively hinders the growth of chromium precipitate phases, ensuring a more uniform distribution of precipitates and further strengthening the alloy. Notably, zirconium has minimal impact on the alloy's electrical conductivity. Firstly, CuCrZr's remarkable heat resistance and superior strength enable it to maintain its integrity and stability in high-temperature environments, making it an ideal material for manufacturing components exposed to extreme temperatures, such as aerospace engine nozzles and components for ITER. Secondly, this alloy demonstrates excellent resistance to oxidation, corrosion, and erosion caused by high-temperature gases. This exceptional property has facilitated its widespread application in various corrosive environments, including chemical equipment, marine engineering, and the nuclear industry. Thirdly, CuCrZr alloys are renowned for their outstanding electrical and thermal conductivity, making them highly suitable for the production of electrical components and heat sinks. Finally, CuCrZr alloys exhibit favorable machinability and can be shaped using various additive manufacturing methods, including L-PBF and LP-DED. Furthermore, they can be welded to other metals.

Progress This review comprehensively examines the forming behavior, microstructure, and overall performance of CuCrZr alloys across three distinct areas. Firstly, it highlights the need to consider the laser absorption rate in addition to the traditional volumetric energy density when evaluating CuCrZr alloys' response to laser processing. This is because the absorption of copper and its alloys significantly varies with the laser wavelength, as illustrated in Fig. 3 and Table 2. Secondly, the review discusses the densities and process parameters of CuCrZr alloys printed using lasers of various wavelengths, further emphasizing the importance of considering absorption rate (Fig. 5 and Table 2). Moreover, the review delves into three types of defects commonly encountered in L-PBF, particularly those that tend to occur during the fabrication of CuCrZr alloy components (Fig. 6). It also examines the variations in the alloy's microstructure before and after heat treatment, along with the underlying causes of these changes (Figs. 8–16). This analysis provides valuable insights into the microstructure evolution and its impact on alloy performance. Additionally, the review explores the impact of an enhanced heat treatment routine and process parameters on the mechanical properties of CuCrZr alloys, as presented in Table 3. Furthermore, it investigates the correlation between densification, heat treatment regimen, and both electrical (Fig. 19 and Table 4) and thermal (Fig. 20 and Table 5) properties.

Conclusions and Prospects This review presents an overview of the current status of the research on CuCrZr alloys in relation to their forming behavior, microstructure, and mechanical, thermal, and electrical properties.

1) The majority of E_A values obtained using near-infrared lasers are lower than those obtained using green lasers. This difference can be explained by the absorption rate of the CuCrZr alloy, which is significantly higher for green lasers compared to near-infrared lasers. Notably, the absorption rate of the CuCrZr alloy decreases monotonically as the laser wavelength increases. A particularly

sharp decrease is observed when the laser wavelength exceeds 550 nm. When comparing the CuCrZr alloy processed with green lasers to that processed with near-infrared lasers, it is evident that the former exhibits a narrower range of density fluctuations. However, the overall density is lower, indicating the potential for further optimizing the green laser process parameters. Common and challenging defects encountered during the LAM of CuCrZr alloys include pores, cracks, and unfused powder.

2) ST modifies the melt pool boundary and grain morphology of the alloy, whereas DAH generates precipitates that bolster its mechanical properties. The L-PBF method yields a CuCrZr alloy rich in supersaturated Cr and Zr atoms within the matrix, owing to the solid solution. Subsequently, DAH triggers precipitation within this matrix, primarily forming Cr, Cu_xZr_y , and Cr_2Zr precipitates. These micro- and nano-sized precipitates significantly enhance the alloy's mechanical properties. However, as the treatment temperature rises, the precipitate distribution transitions from uniform to partially concentrated. Specifically, aging treatments at 500 °C for 2 hours or 550 °C for 1 hour attenuate the {111} and {200} crystal plane orientations while strengthening the {220} crystal plane orientation in the CuCrZr alloy.

3) In as-built state, the CuCrZr alloy demonstrates relatively weak mechanical properties, with yield strengths ranging from 175.2 MPa to 400.0 MPa, ultimate tensile strengths between 254.6 MPa and 447.0 MPa, and elongations varying from 10.0% to 49.4%. However, it is noteworthy that by utilizing green lasers, it is possible to fabricate an as-built CuCrZr alloy with superior mechanical properties. Among various methods, direct aging treatment stands out as the most effective means to enhance these mechanical properties. This treatment achieves optimal results when conducted at approximately 500 °C. Subsequently, the CuCrZr alloy undergoes significant improvements in its mechanical properties after this aging treatment. Specifically, yield strengths increase to range from 361.0 MPa to 527.0 MPa, ultimate tensile strengths improve to fall between 466.0 MPa and 612.0 MPa, and elongations enhance to vary from 12.3% to 21.8%. These remarkable improvements in the mechanical properties of the CuCrZr alloy can be attributed to the formation of precipitates during direct aging treatment, along with a reduction in both dislocation density and thermal residual stress.

4) The CuCrZr alloy, in its as-built state, demonstrates electrical conductivity ranging from 21% IACS to 30.0% IACS and thermal conductivity varying between 100.0 W/(m·K) and 307.0 W/(m·K). This range of conductivities is primarily attributed to the presence of numerous oversaturated Cr and Zr atoms within the alloy matrix. These atoms cause lattice distortion in the grains, which enhances the scattering effect on free electrons. Consequently, the alloy exhibits lower electrical and thermal conductivities. To enhance both electrical and thermal conductivities, the most effective heat treatment process is SAAH. This process, performed at temperatures ranging from 950 °C to 1000 °C followed by an additional 500 °C, significantly improves the conductivity values. Specifically, it elevates the electrical conductivity to a range of 84.0% IACS to 88.1% IACS and boosts the thermal conductivity to levels between 297.0 W/(m·K) and 350.0 W/(m·K). Additionally, the combination of solution annealing and age hardening treatment effectively reduces dislocation density and residual stresses within the alloy. This treatment also produces precipitates, which collectively contribute to further enhancing the electrical and thermal conductivities of the CuCrZr alloy.

The following are anticipated to be the future research prospects and development directions for CuCrZr alloys.

1) Optimization of the process parameters of green laser processing and conducting a comparative analysis of the microstructure and properties achieved through green laser processing and near-infrared laser processing. Fabrication of CuCrZr through the implementation of hybrid laser systems (blue/green laser + NIR laser).

2) The traditional volumetric energy density used in the optimization study of the process parameters still has large limitations because it does not take into account the characteristics of the material. There is an urgent need for a method that can comprehensively consider the material properties and LAM process parameters.

3) Currently, the ideal equilibrium between tensile strength and ductility has yet to be determined, and the amalgamated thermal and electrical characteristics remain unclear. Moreover, the mechanical, electrical, and thermal features have not been sufficiently and comprehensively explored.

4) The EB-PBF method has been used to produce an equiaxed copper alloy containing nickel, aluminum, and bronze (C63000). This alloy boasts isotropic mechanical properties and high levels of strength and elongation. There is potential in the future to produce CuCrZr alloys with an equiaxial grain structure.

Key words laser additive manufacturing; CuCrZr alloy; formation; microstructure; comprehensive properties